Journal of the
Meteorological
Society of
Japan

EARLY ONLINE RELEASE

The DOI for this manuscript is
DOI:10.2151/jmsj.2023-003
J-STAGE Advance published date: October 14th, 2022

Development of a Line-by-line and a Correlated k-distribution Radiation Models for Planetary Atmospheres

Yoshiyuki O. TAKAHASHI

Department of Planetology, Kobe University, Japan
Center for Planetary Science, Kobe University, Japan

and

Yoshi-Yuki HAYASHI

Department of Planetology, Kobe University, Japan
Center for Planetary Science, Kobe University, Japan

and

George L. HASHIMOTO

Department of Earth Sciences, Okayama University, Japan

and

Kiyoshi KURAMOTO

Department of Cosmosciences, Hokkaido University, Japan

and

Masaki ISHIWATARI

Department of Cosmosciences, Hokkaido University, Japan

September 26, 2022

Corresponding author: Yoshiyuki O. Takahashi, Department of Planetology, Kobe University, 1-1, Rokkodaicho, Nada-ku, Kobe 657-8501, Japan.
E-mail: yot@gfd-dennou.org

Abstract

A set of line-by-line and correlated *k*-distribution radiation models are developed aiming for applications in simulations and examinations of Venus and Mars-like planetary atmospheres. Our line-by-line model is validated by comparing the results with observations and those of previous studies under conditions of Venus, and present and possible early Mars. The radiation fields calculated by our line-by-line model agree well with observed profiles and are within the acceptable range from those presented in previous studies. The results obtained by our line-by-line model are then processed to generate a series of parameters for our correlated *k*-distribution model. It is confirmed that the radiation fields calculated with those sets of parameters by our correlated *k*-distribution model sufficiently agree with those by our line-by-line model for the atmospheres with a wide range of surface pressure. By the use of our correlated *k*-distribution model implemented with those sets of parameters, we evaluate the radiation field for Venus and calculate radiative-convective equilibrium profiles for Venus and Mars. The obtained vertical thermal structures for Venus are qualitatively consistent with observations, and the behaviors of surface pressure and surface temperature for Mars are similar to those reported by previous studies. Those results demonstrate that our models including the procedure for generating tables of radiation parameters are applicable to examine climates of CO_2 dominant atmospheres in our solar and exoplanetary systems.

Keywords radiation; planetary atmosphere; Venus; Mars

1. Introduction

Atmospheres and climate systems of planets in the solar system and plausible exoplanets have been studied using various kinds of numerical models. In recent years, while three dimensional simulations by using general circulation models (GCMs) have been vigorously performed, one dimensional radiative-convective equilibrium models are still useful to understand the atmospheric structures and are important to develop and improve GCMs of unknown atmospheres. The core issue in these studies is radiative transfer calculation. Here in this study, we develop a set of line-by-line and correlated *k*-distribution radiation models. Sets of radiation parameters for the correlated *k*-distribution radiation model which can be used in various atmospheric models from one dimensional radiative-convective models to GCMs are composed by the aids of line-by-line calculations. Our aim is to prepare a sequence of procedure and a unified set of tools to generate a series of radiation parameters, and to verify them in the same manner for the atmospheres of Venus and Mars to demonstrate their applicability for considering CO_2 dominant atmospheres including exoplanets.

One of the difficulties in calculating radiative transfer of planetary atmospheres is the uncertainty in radiative properties of possible atmospheric components. An important issue we consider here is to synthesize radiation parameters for thick atmospheres like those of Venus or possible early Mars. One of the most important unknown radiative properties especially for thick atmospheres is absorption coefficient of continuum. Fortunately, experimental studies have provided useful data on optical properties of gases in the conditions of planetary atmospheres. For examples, Gruszka and Borysow (1997) and Baranov et al. (2004) provided absorption coefficients of collision induced absorption (CIA) of CO_2. Those data opened the ways to perform more reliable calculations of radiative transfer in thick CO_2 atmospheres. We also utilize those data here for synthesizing radiation parameters for calculating varieties of thick CO_2 atmospheres.

Another difficulty in calculating radiative transfer is that huge computer resources tend to be required. This is a traditional problem common to the atmosphere of all planets including that of Earth. It is not realistic to perform so called line-by-line integration of radiative transfer in GCMs. One of the ways to avoid this difficulty especially in simulation models is to use the correlated k-distribution method, which efficiently reduces the degree of freedom in wavenumber space of radiative transfer and achieves economical usage of computational resources. Moreover, the method can provide more accurate radiative flux than classical band models and has been widely used in massive computations such as operational weather forecasts and climate studies with GCMs for Earth's atmosphere. Here, we also adopt the correlated k-distribution method to obtain radiation parameters of the radiative transfer models for simulations of planetary atmospheres.

Recently, several open source codes are developed to calculate high resolution spectra of radiation properties of arbitrary planetary atmospheres within the permitted choice of atmospheric composition. The kspectrum (Eymet et al. 2016) and the EXOCROSS (Yurchenko et al. 2018) generate high resolution spectra and thermodynamic properties from given physical tables of atmospheric constituents. Products from those codes have been used for high resolution calculations of radiative transfer of planetary atmospheres (e.g., Ito et al. 2020) and for generation of radiation parameters for low resolution radiative transfer models in GCMs for planetary atmospheres (e.g., Turbet et al. 2018). Irwin et al. (2008) developed NEMESIS (Non-linear optimal Estimator for MultivariatE Spectral analySIS), a high resolution radiative transfer and retrieval code. NEMESIS was originally developed for analysis of spacecraft observations in general, and was used to interpret the Cassini data, and then it has been used to analyze energy budget of various planetary atmospheres (Read et al. 2016). As for the economical radiative transfer models for numerical simulations, various radiation models were developed to be implemented in GCMs for planetary atmospheres (e.g., Hourdin 1992; Eymet et al. 2009; Mischna et al. 2012). However, these models have been developed for respective particular planetary atmospheres. The radiative transfer models and radiation parameters implemented there can be applied to respective limited targets.

In this study, we do not use those existing open source codes to synthesize high resolution spectra or to calculate radiative transfer. We coherently develop two types of radiative transfer models, a line-by-line model and a correlated k-distribution model, which can be used for calculating radiative transfer of a variety of planetary atmospheres and improving the models themselves. The line-by-line model generates high resolution radiation properties in wavenumber space from given data of radiation properties of selected atmospheric constituents, and integrate radiative transfer to produce atmospheric radiation spectra. The correlated k-distribution model generates radiation parameters by the use of correlated k-distribution method with k-distributions synthesized by the line-by-line model, and integrate radiative transfer economically to calculate atmospheric radiation rapidly. The formulations of the models are standard, but they are designed in a similar coding manner to facilitate their interoperable usage. Our aim is to prepare a set of tools which enable us to calculate consistently the radiation parameters for the economical radiative transfer model for the atmosphere from the detailed radiation properties of given atmospheric constituents. The line-by-line model is also used to verify the performance of the correlated k-distribution model with the generated set of radiation parameters. The parameters for the correlated k-distribution model are thus iteratively determined. With the combination of these two radiation models, both an accurate estimate of radiation spectra and a rapid and qualified calculation of radiation field can be ensured. The consistent development of the sequence of procedures is essential for parameter studies of an atmosphere by changing its constituent. By the combination of these two radiation models we can cover a wide range of planetary atmospheres, such as Venus, present Mars, and possible early Mars.

In Section 2, the line-by-line model developed in this study are described. The development of our correlated k-distribution model is described in Section 3. In Sections 4 and 5, the models are applied to Venus and Mars, respectively. The line-by-line model calculations are performed and the results are compared with observations and those of the models developed by other groups. Then, the correlated k-distribution models are developed for each planetary atmosphere, and evaluate the radiation field for Venus and calculate radiative-convective equilibrium profiles for Venus and Mars to demonstrate that the developed model can be well applied to those planetary atmospheres. The obtained vertical thermal structures for Venus are qualitatively consistent with observations, and the behaviors of surface pressure and surface temperature for Mars are similar to those reported by previous studies. Conclusion is presented in Section 6.

2. Description of the line-by-line model

In this section, a line-by-line model developed in this study is described.

2.1 Radiative transfer equation

Radiative fluxes are calculated by the use of the radiative transfer equation with the generalized two-stream approximation (Meadows and Weaver 1980). The approximated equation is solved with the method of Toon et al. (1989). Radiative flux is evaluated as the sum of two fields. Radiation field produced by incident solar radiation is calculated by δ–Eddington approximation. Radiation field produced by emission from the surface and atmosphere, i.e., planetary radiation, is calculated with the hemispheric mean approximation and the source function technique described by Toon et al. (1989) is used. In this study, a word "planetary radiation" stands for radiation calculated with surface and atmospheric emissions, but with no incident solar radiation. A word "solar radiation" stands for radiation with incident solar radiation, but with no surface nor atmospheric emissions.

2.2 Optical properties

Optical properties required to solve the radiative transfer equation are optical depth, single scattering albedo, and asymmetry factor. Here, the calculation of optical depth is described briefly. The details of the optical properties are presented in the supplementary materials.

The optical depth is expressed as sum of those of gas and particles, and the gas' component is sum of four terms expressed with the absorption coefficient of absorption line, the absorption coefficient of continuum, the "absorption cross section", which is a cross section for absorption which is not described by a line absorption nor a continuum absorption, and the Rayleigh scattering coefficient. The absorption coefficient of absorption line at a wavenumber is calculated as the product of a line intensity, a line shape function, and a line cutoff function, as shown in (S.7) in supplementary materials. The functional forms of the line cutoff function are described in Appendix A, and the cutoff widths used in the calculations are described in Sections 4.1 and 5.1 for Venus and Mars, respectively.

2.3 Optical data sources

In calculation of absorption coefficients, gas absorption line parameters are obtained from HITRAN (high-resolution transmission molecular absorption database), such as HITRAN2012 (Rothman et al. 2013). As for calculation in high temperature condition, absorption line parameters are given by HITEMP2010 (Rothman et al. 2010).

Continuum absorption is evaluated by a combination of following models. Absorption coefficient of water vapor continuum is obtained by the MT_CKD model (Mlawer et al. 2012). The version 3.0 of the MT_CKD model is used in this study. For thick CO_2 atmospheres, such as the atmospheres of Venus and possible early Mars, CIA is considered (see Sections 4.1 and 5.1). “Absorption cross section” is obtained by several sources. Details are described in Section 4.1.

Rayleigh scattering coefficients for air and CO_2 are obtained from Hansen and Travis (1974). Rayleigh scattering coefficients for H_2O, N_2, O_2, and CH_4 are calculated by the use of the coefficient for air with multiplying factors for individual species (Pierrehumbert 2010) (Table 1). Rayleigh scattering coefficients of other species including radiatively inert component are assumed to be the same as that of air. Table 1

The extinction efficiency factor, single scattering albedo, and asymmetry factor of particles are obtained from previous studies. Details are described in Sections 4.1 and 5.1 for each planetary atmosphere.

3. Description of the correlated *k*-distribution model

In this section, correlated *k*-distribution model developed in this study is described. The radiative transfer equation used in the correlated *k*-distribution model is the same as that in the line-by-line model (Section 2.1), and the methods to solve the equation are also the same as those used in the line-by-line model.

3.1 Overview of the model

In a correlated *k*-distribution method, first, overall spectrum region is divided into bands. The wavenumber boundaries of the bands are determined based on the spectra of target atmosphere. It is also considered that the band width is narrow enough that the Planck function and the incident solar irradiance do not change greatly within the band. Then, the absorption coefficient as a function of wavenumber is sorted in ascending order in each band with an assumption of correlation between absorption coefficients at different altitude levels. By sorting absorption coefficient, number of integration points required for wavenumber integration can be decreased greatly compared to the line-by-line method without significant loss of accuracy. Then, the wavenumber space for each band is transformed into cumulative probability space from 0 to 1. In our correlated k-distribution model, we divided the cumulative probability space into two regions to express the sharpness of the distribution as is similar to the model developed by Mischna et al. (2012). In this study, however, one of the two regions ranges from 0 to 0.98 and the other ranges from 0.98 to 1. The boundary between two regions (0.98) is different from that used by Mischna et al. (2012), which is 0.95. We found that the correlated k-distribution model with the boundary at 0.98 produces radiation fields closer to those by the line-by-line model than does the correlated k-distribution model with the boundary at 0.95. In the numerical integration over cumulative probability space, the Gaussian quadrature is applied in each region. In addition, we consider correlations of gas absorption coefficient with the Planck function and the solar flux by sorting the Planck function and the solar flux by the order of the gas absorption coefficient (Mlawer et al. 1997).

In our correlated k-distribution model, absorption coefficients of gases at jth integration point in ith band, $k_{i,j}$, is a function of pressure, temperature, and composition. The absorption coefficients for arbitrary values of pressure, temperature, and composition are obtained by interpolating the values that have been pre-calculated and tabulated for sets of values of pressure, temperature, and composition. Here, linear interpolations in temperature, logarithm of pressure, and logarithm of volume mixing ratio are adopted. In treating atmospheric composition, we have two kinds of gas species. One is "key species", whose line overlap is explicitly considered. Absorption coefficients of those are summed in wavenumber space and total absorption coefficient is sorted in each band as described above. The other is "non-key species", whose line overlap is considered by using the absorption coefficients averaged over each cumulative probability region represented by each integration point. The absorption coefficient of non-key species is sorted by the order of the key species' absorption coefficient, and is averaged. The pre-calculated values for key species are stored in the table which has axes of pressure, temperature, and volume mixing ratios of up to three key species. For example, absorption coefficient at jth integration point in ith band, $k_{i,j}(p_l, T_m, r_{1,n_1}, r_{2,n_2}, r_{3,n_3})$, is stored at discrete pressure p_l, temperature T_m, and volume mixing ratio $r_{1,n_1}, r_{2,n_2}, r_{3,n_3}$ grids, where l, m, n_1, n_2, n_3 are indexes for each variables. On the other hand, the pre-calculated values for non-key species are stored in the table, but only the axes of pressure and temperature are utilized.

Rayleigh scattering coefficients and optical properties of particle species are also calculated in advance, and stored in the table. Those values are obtained by averaging the line-by-line values in each band. The method for average is described in Appendix B.

3.2 Generating k-distribution tables

We generate tables for correlated k-distribution models by processing the optical properties calculated by our line-by-line model (Section 2) as described above. As a result of the process, the developed correlated k-distribution model has two kinds of errors.

In a correlated k-distribution model, a spectrum of radiative flux is divided into a finite number of bands whose wavenumber interval is transformed into cumulative probability space from 0 to 1, and for each band, cumulative probability space is further divided into a finite number of integration points, at which the radiative transfer equation is integrated by using the sorted value of absorption coefficient. Absorption coefficients for arbitrary values of pressure, temperature, and composition are calculated by interpolating pre-calculated values at selected grids of the set of pressure, temperature, and volume mixing ratios of composition in the table. Reduction of the number of bands and the number of integration points in each band contributes to saving computer resources, but becomes a source of errors. Reduction of the number of grids for pre-calculated values in the table contributes to lightening preprocessing efforts, but also becomes a source of errors. In generating tables, these two kinds of errors are also evaluated sequentially, as follows.

First, a line-by-line calculation is performed by the use of a reference atmospheric profile; spectral profiles of gas absorption coefficients and a spectrum of particle optical property are synthesized, and the spectrum of a solar insolation is prepared. Then, by the use of the spectra, a number of k-distributions with a variety of numbers of bands and integration points are generated, and radiative fluxes, flux convergences, and temperature tendencies are calculated by using them. Based on the differences, i.e., root mean square errors (RMSEs), between results of the k-distribution calculations and the line-by-line calculation for the reference atmospheric profile, the numbers of bands and integration points which are reasonably sufficient for the k-distribution table to reproduce the line-by-line result are determined. After this procedure, the number of integration points in each band is decreased by checking differences to find a set of decreased number of integration points which does not result in significant loss of accuracy in the calculated radiation field. It should be noticed that the k-distribution calculations here and obtained tables are "exact" in the sense that they are calculated directly for a given reference atmospheric profile.

Second, a number of line-by-line calculations are performed at grids of the set of pressure, temperature, and volume mixing ratios encompassing the reference atmospheric profile with a variety of pressure, temperature, and volume mixing ratio intervals, and k-distribution tables are generated with the fixed numbers of bands and integration points determined above. Then, the appropriate intervals for pressure, temperature, and volume mixing ratios grids of the table are determined based on differences, i.e., RMSEs, between results of the k-distribution calculations and the line-by-line calculation for the reference atmospheric profile. In this study, the intervals for pressure and temperature are judged to be appropriate if the RMSEs are smaller than 1.5 times those of the k-distribution calculation without interpolation compared to the line-by-line calculation.

In this study, the target accuracy of the correlated k-distribution model is determined by the uncertainty of the other radiation models which have been used in the studies of planetary climate. The values of target accuracy are described in Sections 4.2 and 5.2 for Venus and Mars, respectively. Note that the accuracy set in this study is, however, temporal target. Determining the accuracy itself is one of the issues in studies not only of the present climates of Venus or Mars, but also of planetary climates in general, and will be determined iteratively by performing the calculations and by improving the models during the course of researches. Therefore, the important issue in this study is to construct a practically useful procedure to generate a table for those researches.

4. Application to Venus

In this section, application of our radiation models to Venus is described. First, line-by-line calculations are performed. Then, the correlated k-distribution model is constructed for Venus. Finally, radiation field is evaluated, and radiative-convective equilibrium calculations are performed to demonstrate behavior of the developed model.

4.1 Line-by-line model calculation

We perform the line-by-line calculation for Venus, and compare the results with available observation to validate the model.

Table 2

Table 3

Line absorption parameters used in calculations for Venus atmosphere are obtained from HITRAN2012 (Rothman et al. 2013) and HITEMP2010 (Rothman et al. 2010). The line parameters of HITEMP2010 are used for H_2O, CO_2, and CO, but lines with intensity less than 10^{-38} cm^{-1} (molecule $cm^{-2})^{-1}$ are excluded to save computational time. The exclusion of such weak lines has little influence on the results in this study (not shown). The isotope ratios of Earth's atmosphere are assumed in this study. Cutoff widths of absorption line calculation are assumed to be 250 cm^{-1} for CO_2, 25 cm^{-1} for H_2O, and 100 cm^{-1} for other species (Lee et al. 2016). The results presented in this study are not sensitive to the cutoff width. If the cutoff width for the CO_2 is changed, for example, to 500 cm^{-1}, the changes in radiative fluxes are less than 0.2 W m^{-1}. Air-broadened half width of H_2O is multiplied by a factor of 1.7 to consider effects of collisions with CO_2 (Fedorova et al. 2008). The MT_CKD model (Mlawer et al. 2012) is used to evaluate continuum absorption by H_2O. In addition, CIAs of CO_2, and SO_2 absorption described as "absorption cross section" are included (Tables 2 and 3). Rayleigh scattering is considered as described in Section 2.3.

In the calculation, the vertical atmospheric profiles for temperature, composition, cloud, and "UV absorber" are specified based on observations. The specified composition includes H_2O, CO_2, SO_2, CO, HF, OCS, and N_2. The assumed cloud is composed of four kinds of particles, i.e., modes 1, 2, 2', and 3, which have different particle sizes. In addition, the UV absorber is assumed to distribute around cloud top. Almost the half of the absorption of solar radiation is caused by the UV absorber, but its composition is not yet determined (Crisp 1986).

The vertical temperature profile is specified based on the low latitude profile of the VIRA (Venus International Reference Atmosphere; Seiff et al. (1985)) (Fig. 1a). Two vertical profiles of atmospheric composition are prepared to check sensitivity. In the profile named A, volume mixing ratios of H_2O, CO_2, and SO_2 are adopted from Crisp (1986), and those of CO, HF, OCS, and N_2, are adopted from Pollack et al. (1993) (Fig. 2a). In the profile named B, volume mixing ratios of all gases are adopted from Pollack et al. (1993) (Fig. 2b). This means that the differences between two profiles are volume mixing ratios of H_2O, CO_2, and SO_2, and the CO_2

volume mixing ratio in profile A, 0.960, is slightly different from that in profile B, 0.965. Hereafter, the calculations with the profile A and with the profile B are referred to as Case $\mathrm{V_A}$ and Case $\mathrm{V_B}$, respectively. Mass mixing ratios of cloud and UV absorber are adopted from Crisp (1986) (Fig. 1b) Optical properties of those cloud are obtained from Crisp (1986, 1989). In this study, radiation fields with one cloud model described above is focused, although the other cloud models such as those by Zasova et al. (2007) and Haus et al. (2013) have been proposed. The sensitivity of the radiation fields on the cloud model, as was shown by Lebonnois et al. (2015), is an interesting future work.

Table 4

The incident solar radiation flux at the top of the atmosphere is assumed to be 2635 W $\mathrm{m^{-2}}$. Solar flux spectrum of Gueymard (2004) is used for the calculation. Surface albedo is set to 0.05 in wavenumber larger than 7700 $\mathrm{cm^{-1}}$, and is zero in smaller wavenumber range. This albedo spectrum is a simplification of observed one shown in Golovin et al. (1983). Gravitational acceleration and specific heat at constant pressure are listed in Table 4. Line-by-line calculations with wavenumber resolution of 0.1 $\mathrm{cm^{-1}}$ are performed with 80 atmospheric layers (81 levels) up to 2.66 Pa pressure level based on the VIRA. Wavenumber resolution of 0.1 $\mathrm{cm^{-1}}$ is not enough to resolve all absorption lines fully. But, it is enough in comparing the results with available observations, and in constructing the correlated *k*-distribution model for Venus.

Fig. 1

Fig. 2

From Fig. 3 to Fig. 7, results of Venus calculations are presented. The radiation fields calculated by our model show features similar to those revealed by observations as follows. Figure 3 shows longwave net flux profiles calculated by our model and the fluxes observed by the Pioneer Venus probes (Revercomb et al. 1985). Calculated fluxes for Cases $\mathrm{V_A}$ and $\mathrm{V_B}$ are both within the range of the observed values. Range of the observed net flux is considered to be caused by latitudinal variation of water vapor amount (Revercomb et al. 1985). It is qualitatively consistent with our results, in which radiative flux would vary if atmospheric water vapor abundance varies as large as several hundreds ppmv. Figure 4 shows shortwave (0.4–1.0 μm) flux profiles at a solar zenith angle of 65.6° calculated by our model and the fluxes observed by the Pioneer Venus probe (Tomasko et al. 1980a). The fluxes for Cases $\mathrm{V_A}$ and $\mathrm{V_B}$ are well agreed with observations over almost all altitude though the fluxes for Case $\mathrm{V_B}$ are slightly larger than those for Case $\mathrm{V_A}$. Figure 5 shows net shortwave flux at the surface as a function of solar zenith angle calculated by our model and the fluxes observed by several missions (Marov et al. 1973; Moroz et al. 1985). Although the observed values are scattered largely, general trend of the solar zenith angle dependence is reproduced by our model. Figure 6 shows planetary albedo spectra calculated by our model and observed albedos (Moroz et al. 1985). Gross feature of observed wavelength dependence of albedo is represented by our model in visible and near infrared region in Case V_A, though the calculated albedo in near infrared region is slightly lower than observed value. Albedo in Case V_B is almost the same as that in Case V_A, except for wavelength shorter than 0.35 μm. In this shorter wavelength region, albedo in Case V_B is larger than that in Case V_A and observation. This is attributed to the low SO_2 concentration. Figure 7 shows the calculated near infrared upward radiative flux spectra at the top of the atmosphere in nightside. Thermal emission windows in the near infrared wavelengths observed by ground-based and spacecraft observations (e.g., Allen and Crawford 1984; Titov et al. 2007) are well reproduced.

Fig. 3

Fig. 4

Fig. 5

Fig. 6

Fig. 7

Table 5

4.2 k-distribution table

We generate a *k*-distribution table for Venus by using the line-by-line model described in Section 4.1. The composition profile of Venus atmosphere here is fixed to be that of Case V_A (Fig. 2a) described in Section 4.1. This means that the key species of the table is a virtual gas whose optical properties are the same as those of Venus atmosphere with assumed composition. The distribution of cloud used in the line-by-line calculations described in Section 4.1 (Fig. 1b) is used to evaluate the errors of a correlated *k*-distribution model. In this study, the developed correlated *k*-distribution model is evaluated based on the RMSEs of radiative fields compared to those of the line-by-line model over all altitude ranges, and the value of target accuracy for Venus is set to $\sim 2\times10^{-4}$ W m^{-3} for flux convergence of planetary radiation. The target is based on an uncertainty of the radiation model developed by Eymet et al. (2009). It is one of the pioneering models in a successful application to GCM simulations of Venus atmosphere (e.g., Lebonnois et al. 2010). In the followings, the *k*-distribution table generated for Venus is described. The details of the generation process can be found in supplementary materials.

The generated *k*-distribution table has 26 bands and variable number of integration points for each band as is shown in Table 5. The *k*-distributions are generated at grids of 91 pressure values from 10^{-1} Pa to 10^{8} Pa with interval of $\Delta(\log_{10} p) = 0.1$ and zero Pa, and 17 temperature values from 100 K to 900 K with interval of $\Delta T = 50$ K.

Fig. 8

Figure 8 shows comparison of global mean radiative fluxes, flux convergences, and temperature tendencies between the line-by-line calculation and the k-distribution calculation with the generated table. In order to evaluate the global mean of solar radiation flux, radiative fluxes are calculated at two solar zenith angles of 37.9° and 77.8°, and are averaged, and halved considering the non-contribution of nightside. It is noted that those solar zenith angles correspond to points required for the Gaussian quadrature for dayside. Incident solar radiation flux, its spectrum, and surface albedo are the same as those described in Section 4.1. The results of the k-distribution calculation are very close to those of the line-by-line calculation. The RMSEs evaluated over all altitude ranges are shown in Table 6. The RMSE of the flux convergence in planetary radiation is smaller than the value of target accuracy set in this study.

Table 6

4.3 Radiation field for the VIRA

Radiative fluxes at the top of the atmosphere and the surface, the vertical and the meridional distributions of radiative heating rate for the VIRA are evaluated by the use of our correlated k-distribution model. Temperature is horizontally uniform below 8×10^5 Pa level (about 32 km altitude). Around 10^4 Pa level (about 64 km altitude), a minimum which is known as "cold collar" is found in middle latitude. Temperature increases with increasing latitude above about 10^3 Pa level (about 76 km altitude). In the calculations, meridional distribution of temperature is obtained from the VIRA and the temperature is assumed to be zonally uniform. The distributions of gas and cloud are assumed to be horizontally uniform with the vertical profiles described in Section 4.1. The vertical distribution of gas is that of Case $\mathrm{V_A}$ (Fig. 2a). In order to evaluate the diurnal mean of solar radiation flux, radiative fluxes are calculated at two hour angles of 19.0° and 71.0°, and are averaged, and halved considering the non-contribution of nightside.

Table 7 shows global mean radiative fluxes at the top of the atmosphere and the surface for the VIRA obtained by the k-distribution calculation. Although we used the distributions of composition and cloud, and the optical properties described in Section 4.1 without any tuning, the calculated global mean values are close to observed values. The calculated outgoing planetary radiation is 154.3 W m^{-2}, which agrees with observation (157.0±6.9 W m^{-2}) (Schofield and Taylor 1982). The calculated solar radiation absorbed by the surface is 16.5 W m^{-2}, which agrees well with observation (∼17 W m^{-2}) (Tomasko et al. 1980a). The calculated planetary albedo (=UpSR/DnSR at TOA) is 0.76, which is not far from the observed value (∼0.80±0.02) (Tomasko et al. 1980b), and agrees well with an estimation based on a radiative-convective equilibrium calculation (0.76) (Read et al. 2016).

Figure 9 shows meridional distributions of diurnal mean net radiative fluxes at the top of the atmosphere and the surface for the VIRA. Planetary radiation flux at the top of the atmosphere is almost uniform with a slight decrease and a slight increase in middle and high latitudes, respectively, while solar radiation flux decreases monotonically from the equator to the pole. These distributions are consistent with observations (e.g., Taylor et al. 1983; Schubert 1983), though the composition and the cloud are assumed to be horizontally uniform in this calculation. Our result shows that the solar radiation flux absorbed by the surface is 22 W m^{-2} at the equator.

Figures 10–13 show temperature tendencies and flux convergences for the VIRA calculated by the models developed in this study. In the followings, it is demonstrated that the model developed in this study behaves well by describing that the features of the tendency distributions obtained by our model are overall in agreement with those presented by previous studies (e.g., Lebonnois et al. 2015; Haus et al. 2015). Figure 10 shows vertical profiles of global mean temperature tendency and flux convergence for the VIRA. Just above the surface, there is a shallow layer of 1–2 km thickness, 1–2 model layers, with intense planetary radiation cooling (Fig. 10b). Above the layer up to about 10^5 Pa level, the atmosphere is heated by solar radiation absorption with intensity of about 2×10^{-3} W m^{-3}. The layer is cooled by planetary radiation in average, though the cooling rate profile shows fluctuation due to very small temperature fluctuation of the VIRA. Around 10^5 Pa level, at cloud base, there is a thin layer with intense planetary radiation heating which is caused by the absorption of radiation emitted by the lower layers (Lebonnois et al. 2015). Above the layer, the atmosphere is heated by solar radiation with a bump around 10^4 Pa level due to the presence of UV absorber (Lebonnois et al. 2015; Haus et al. 2015).

Figure 11 shows meridional distributions of temperature tendency for the VIRA. Above about 10^5 Pa level (about 50 km altitude), there appears a region of planetary radiation cooling of the amount of 10–18 K day^{-1} in high latitudes. This strong planetary radiation cooling occurs because of temperature in high latitude higher than that in low latitude above the poleward region of “cold collar”. Total temperature tendency is positive in low latitude around 10^4 Pa level and above about 10^3 Pa level. These features are similar to those presented by Haus et al. (2015).

Figures 12 and 13 show radiative temperature tendency spectra as a function of altitude for planetary radiation and solar radiation, respectively. These are evaluated by the use of our line-by-line model for low latitude temperature profile of the VIRA at the condition of zero solar zenith angle. In Fig. 12, cooling appears in the wide range of altitudes in the thermal infrared wavelengths; the most intense one appears above about 10^3 Pa level caused by CO_2 15 μm band. At the bottom of the cloud layer around 10^5 Pa level, heating occurs in near infrared wavelengths. This is a spectral appearance of global mean planetary radiation heating caused by absorption of radiation emitted from the hot lower atmosphere (Fig. 10). Figure 13 indicates that solar radiation heating in cloud layer mainly occurs due to absorption of solar visible radiation around 10^4 Pa level, where UV absorber layer is located (Fig. 1b). This heating causes the bump found in Figs. 10 and 11. Solar near infrared radiation contributes heating in a wide range of altitude in and above the cloud layer. These features are also consistent with those presented by previous studies (Lebonnois et al. 2015; Haus et al. 2015).

Table 7

Fig. 9

Fig. 10

Fig. 11

Fig. 12

Fig. 13

4.4 Radiative-convective equilibrium

A simple one dimensional radiative-convective model with the correlated *k*-distribution model described above as the radiative transfer model is integrated to obtain the equilibrium structures of the atmosphere under the conditions of Venus. The dry convective adjustment is applied when the lapse rate is greater than the dry adiabatic lapse rate. In this study, a constant dry adiabatic lapse rate is used in the adjustment. In addition, a weak vertical filter of simple second-order diffusion form with a coefficient of 10^{-3} is included in the model to avoid vertical two-grid interval noise. The two-grid interval noise occurs in the case with the vertical layer arrangement which does not fit the boundary of the surface convection layer. It was checked that the thermal structure obtained with the filter is compared well with that obtained with vertical layer arrangement adjusted to fit the convection layer and without the filter. The surface temperature is assumed to be the same as that of atmosphere just above the surface due to the convection. Incident solar radiation flux, its spectrum, and surface albedo are the same as those described in Section 4.1. In order to emulate the global mean structure, the global mean solar radiation fluxes are evaluated with the method same as that described in Section 4.2. The values of gravitational acceleration and specific heat at constant pressure are listed in Table 4. The initial condition is adopted from the low latitude profile of the VIRA. In the time integration, the vertical profiles of composition and cloud are fixed to those described in Section 4.1. Calculations are performed for both of gas composition profiles shown in Fig. 2. Two calculations are referred to as Case $\mathrm{V_A}$ and Case $\mathrm{V_B}$ as in Section 4.1. In the Case $\mathrm{V_B}$, a k-distribution table generated in the same manner as that for Case $\mathrm{V_A}$ is used. The model has 80 atmospheric layers (81 levels), which are the same as those of radiative calculations in Section 4.1.

After the model is integrated for 1–2$\times 10^5$ Earth days, the model atmospheres are regarded to reach their equilibrium states. Table 8 shows global mean radiative fluxes at the top of the atmosphere and the surface in the equilibrium states. Except for the planetary radiation fluxes at the surface, radiative fluxes in radiative-convective equilibrium are within the range of 10 W $\mathrm{m^{-2}}$ or less from those for the VIRA (Table 7). The values of outgoing planetary radiation and solar radiation absorbed by the surface are close to observed ones, especially for Case V_A (see Section 4.3).

Figure 14 shows the temperature, the temperature difference from the VIRA, and the static stability in the equilibrium states. Temperature tendencies and flux convergences in the equilibrium states are shown in Fig. 15. It should be noticed that the static stability profiles shown in Fig. 14c are estimated by the use of the adiabatic lapse rate of the VIRA, not the constant adiabatic lapse rate used in the model. Comparison with the VIRA should be made carefully, especially for the lower atmosphere because the adiabatic lapse rate is assumed to be constant in the radiative-convective model. We can still recognize several features in the radiative-convective equilibrium profiles, such as a convection layer in middle atmosphere and a highly stable layer below it, which resemble those of the VIRA and radiative-convective equilibrium calculations performed by previous studies (Lee and Richardson 2011; Lebonnois et al. 2015; Mendonça et al. 2015). The equilibrated surface temperature is 730 K, and is not far from the observed values, but it would be affected by the assumption of the model, such as constant specific heat. The sensitivity of the surface temperature on the thermodynamics properties is a target of our next study. A layer whose stability is diagnosed as negative is found around 10^5 Pa level (about 55 km altitude) (Fig. 14c). This layer is neutral with respect to the adiabatic lapse rate estimated with the constant specific heat and the ideal gas law. This is generated by convective adjustment caused by near infrared heating at the bottom of cloud layer (Fig. 12). The existence of the convective layer is well-known and is robustly seen both in all observations (e.g., Seiff et al. 1980; Ando et al. 2020) and in previous model calculations (e.g., Lee and Richardson 2011; Lebonnois et al. 2015).

In addition to the layer with negative stability around 10^5 Pa level, two layers with negative stability are found in Fig. 14c. One of those is found just above the surface. This layer is neutral with respect to the adiabatic lapse rate estimated with the constant specific heat and the ideal gas law, and is generated by convective adjustment caused by imbalance of surface radiative energy budget. The layer is shallow and its thickness is one model layer (1 km). This layer reminds us of the convective surface layer found in a GCM simulation by Lebonnois et al. (2018). The other layer is found around 10^6 Pa level (about 29 km altitude), only in Case $\mathrm{V_B}$. Actually, this layer is stable with respect to the adiabatic lapse rate estimated with the constant specific heat and the ideal gas law, and the layer is in radiative equilibrium with the solar radiation heating of $3–4\times10^{-4}$ W $\mathrm{m^{-3}}$ (Fig. 15b).

It can be observed in Figs. 14 and 15 that the overall structures for Case $\mathrm{V_B}$ is similar to those for Case $\mathrm{V_A}$. However, in the lower atmosphere, the stability for Case $\mathrm{V_B}$ is less than that of Case $\mathrm{V_A}$. The major difference in lower atmospheric composition between two cases is the amount of H_2O. The thickness of the convective layer around 10^5 Pa is also different between two cases. The convection layer in Case $\mathrm{V_A}$ is thicker than that in Case $\mathrm{V_B}$. The major differences in composition around this altitude are the amounts of H_2O and SO_2. Our result indicates that the thermal structure of the lower and middle atmosphere of Venus are sensitive to the amounts of H_2O and SO_2. The assumptions of constant specific heat on constant pressure and equation of state for ideal gas may also affect the calculated thermal structure. The dependence of thermal structure on compositional varieties and thermodynamic properties will be investigated in near future.

Table 8

Fig. 14

Fig. 15

5. Application to Mars

In this section, application of our radiation models to Mars is described.

5.1 *Line-by-line model calculation*

Calculations for Mars atmosphere are performed in three conditions which cover a surface pressure range from 6 hPa (present Mars) to 2 bar (possible early Mars), and the results are compared with those of other models to validate the model. Line absorption parameters used in calculations for the Mars atmosphere are obtained from HITRAN2012 (Rothman et al. 2013). The isotope ratios of Earth's atmosphere are assumed in this study. Cutoff widths of absorption line calculation are assumed to be 500 and 25 cm^{-1} for CO_2 and other species, respectively. The cutoff width for CO_2 follows that of Wordsworth et al. (2010). Air-broadened half width of H_2O is multiplied by a factor of 1.7 to consider effects of collisions with CO_2 (Fedorova et al. 2008). The MT_CKD model (Mlawer et al. 2012) is used to evaluate continuum absorption by H_2O. In addition, CIAs of CO_2 is included (Table 2). Rayleigh scattering is considered as described in Section 2.3. Gravitational acceleration and specific heat at constant pressure are listed in Table 4.

a. 6 hPa atmosphere

Fig. 16

We use the present Mars conditions described by Mischna et al. (2012). They are clear-sky 6 hPa dry and moist atmospheres with surface temperature of 250 K (Fig. 16). Atmosphere is composed of 95.3% CO_2, given amount of H_2O, and radiatively inert N_2. The incident solar radiation flux is assumed to be 588.8 W m^{-2} to have the same incident flux as Mischna et al. (2012). Solar flux spectrum of Gueymard (2004) is used for the calculation. Solar zenith angle is 60°. Surface albedo is set to 0.2 in wavenumber larger than 2222 cm^{-1} and is zero in smaller wavenumber range following Mischna et al. (2012). Line-by-line calculations with wavenumber resolution of 0.01 cm^{-1} are performed with 101 atmospheric layers (102 levels) up to 4.2×10^{-2} Pa pressure level. As is in the Venus case, wavenumber resolution of 0.01 cm^{-1} is enough in this study, although all absorption lines cannot be resolved fully. The atmospheric layers are adopted following Mischna et al. (2012) except for one additional layer at the top of the atmosphere in order to calculate fluxes in the upper layer more accurately.

Figure 17 shows radiative fluxes and temperature tendencies for 6 hPa Mars moist atmosphere calculated by our model. The results of other models shown by Mischna et al. (2012) are also plotted for comparison, by the use of the data provided by them. The radiation models used in comparison are two correlated *k*-distribution models of Mischna et al. (2012) (KDM) and the NASA Ames research center (Haberle et al. 2019) (Ames), a model of Kasting group (Kasting 1991; Pavlov et al. 2000; Haqq-Misra et al. 2008) (Kasting), and the LBLRTM (Clough et al. 2005) only for longwave. As for correlated *k*-distribution models of KDM and Ames, *k*-distribution tables were exchanged and sensitivity was checked. In addition, another radiative transfer equation solver, TWOSTR (Kylling and Stamnes 1995), was also used to check sensitivity of the results. Here, following Mischna et al. (2012), longwave and shortwave stand for 10–2222 cm^{-1} and 2222–41666 cm^{-1}, respectively. The radiative fluxes and temperature tendencies calculated by our model are within the range of results of various models. Our results are close to those of two correlated *k*-distribution models, i.e., KDM and Ames, for longwave radiation, and are between the results of the correlated *k*-distribution models and the Kasting model for shortwave radiation. Absorption of shortwave radiation in our model is slightly larger than those of the correlated *k*-distribution models, but the differences are less than 1%. It may be noticed that the longwave temperature tendency of the LBLRTM is not shown above 2 Pa pressure level. This is because the longwave temperature tendency is inconsistent with the flux convergence in the altitude region with some reason. The radiation fields for 6 hPa Mars dry atmosphere are similar to those for 6 hPa Mars moist atmosphere, except for the region just above the ground due to the different optical thickness. The results calculated by our model compare with those by other models, in the similar way as moist atmosphere case, and are shown in supplementary materials. Fig. 17

b. 500 hPa atmosphere

We use the early Mars conditions described by Mischna et al. (2012). They are clear-sky 500 hPa dry and moist atmospheres with surface temperature of 250 K (Fig. 16). Atmospheric composition is the same as those of 6 hPa atmosphere cases in view of volume mixing ratio profile as a function of normalized pressure. The incident solar radiation flux is assumed to be 441.6 W m^{-2}, which is 75% of the present value to consider the faint young Sun and results in the same incident flux as Mischna et al. (2012). Solar flux spectrum, solar zenith angle, and surface albedo are the same as those used in the 6 hPa atmosphere case (Section 5.1a). Line-by-line calculations with wavenumber resolution of 0.01 cm^{-1} are performed with 100 atmospheric layers (101 levels) up to 8.5×10^{-1} Pa pressure level based on the profile shown by Mischna et al. (2012).

Figure 18 shows radiative fluxes and temperature tendencies for 500 hPa Mars moist atmosphere calculated by our model and other models. The results of the other models for the 500 hPa atmosphere spread more than those for 6 hPa atmosphere. Radiative fluxes calculated by our model is close to those of the Kasting model and are less than those of the correlated *k*-distribution models. As Haqq-Misra et al. (2008) discussed in the intercomparison of radiation models in an early Earth-like condition, the differences in radiation field can arise from a number of factors, such as a different numerical technique and a different treatment of H_2O continuum, and so on. These factors would contribute to the differences between various models shown in Fig. 18. For example, in the Kasting model, the radiative transfer equation is solved by the use of the same method as our model (Pavlov et al. 2000). This would partially explain that our results are close to those by the Kasting model. The results for 500 hPa Mars dry atmosphere is shown in supplementary materials.

Fig. 18

c. 2 bar atmosphere

We use the early Mars condition described by Wordsworth et al. (2010). It is clear-sky 2 bar dry atmosphere composed of pure CO_2 with surface temperature of 250 K. The temperature profile is composed of three layers, a dry adiabatic layer, a CO_2 saturated layer, and an isothermal stratosphere of 167 K up to 2 Pa pressure level (Fig. 16). The condensation temperature of CO_2 is calculated with the equations used by Kasting (1991). The incident solar radiation flux is the same as that in the 500 hPa atmosphere case. Solar flux spectrum, solar zenith angle, and surface albedo are the same as those used in the 6 hPa and the 500 hPa atmosphere cases (Sections 5.1a and 5.1b) except that the surface albedo changes at 2600 cm^{-1}, which is one of band boundaries to be set in a correlated *k*-distribution model described below. Line-by-line calculation with wavenumber resolution of 0.01 cm^{-1} is performed with 46 atmospheric layers (47 levels) up to 2 Pa pressure level with layer thickness of 0.2 scale height.

Planetary radiation fluxes calculated by our model, Wordsworth et al. (2010), and Ramirez et al. (2014) are shown in Table 9. The radiative fluxes by our model differ from those by Wordsworth et al. (2010) and Ramirez et al. (2014) by 1–8 W m^{-2}. It should be noticed that Wordsworth et al. (2010) calculated the radiative flux for the pure CO_2 atmosphere, while Ramirez et al. (2014) calculated that for an atmosphere with 95% CO_2 and 5% N_2. However, this compositional difference does not have an important impact on the results. In fact, we confirmed by calculating the radiative flux for the atmosphere with 95% CO_2 that the 5% difference in CO_2 volume mixing ratio results in radiative flux difference less than 1 W m^{-2}. We also confirm the effect of source function technique (Toon et al. 1989) by calculating the flux without using the method (no SFT (source function technique) in Table 9). The fluxes calculated without source function technique are closer to those by previous studies. The difference between the fluxes calculated with and without the source function technique is caused by the discretization of the radiative transfer calculation, since the source function technique was developed to increase the accuracy for a non-scattering atmosphere by integrating a part of the radiative transfer equation analytically. The method by Toon et al. (1989) is widely used in simulations of Martian atmosphere. It should be noticed that a choice of radiative transfer equation solver may cause uncertainty of ∼5 W m^{-2}.

Table 9

5.2 k-distribution table

Table 10

We generate a *k*-distribution table for Mars by using the line-by-line model described in Section 5.1. In order to treat variable amount of CO_2 and water vapor, accurately, those molecules are treated as key species. Gas absorption line parameters and Rayleigh scattering coefficients used to develop a correlated *k*-distribution model for Mars are the same as those described in Section 5.1. As is the case for Venus, the correlated *k*-distribution model developed in this study is evaluated based on the RMSEs of radiative fields compared to those of the line-by-line model over all altitude ranges for the 500 hPa moist atmosphere described in Section 5.1b. The values of target accuracy for Mars are set to the altitude-averaged half widths between minima and maxima of radiative fluxes and temperature tendencies of other models shown in Section 5.1b. The half widths are 5.8 W m^{-2}, 1.9 W m^{-2}, 1.3×10^{-5} K s^{-1} for upward and downward fluxes, and temperature tendency for planetary radiation, respectively, and 1.3 W m^{-2}, 7.4×10^{-1}

W m^{-2}, 4.2$\times10^{-6}$ K s^{-1}, for those for solar radiation. In the followings, the k-distribution table generated for Mars in this study is described. The details of the generation process can be found in supplementary materials.

The generated k-distribution table has 20 bands and variable number of integration points for each band as is shown in Table 10. The k-distributions are generated at grids of 39 pressure values from 10^{-4} Pa to 10^{4} Pa with interval of $\Delta(\log_{10} p) = 1$, from 10^{4} Pa to 10^{7} Pa with interval of $\Delta(\log_{10} p) = 0.1$ and zero Pa, and 16 temperature values from 100 K to 400 K with interval of $\Delta T = 20$ K, 13 H_2O volume mixing ratio values from 10^{-7} to 10^{-1} with interval of $\Delta(\log_{10} r_{\mathrm{H_2O}}) = 0.5$ and zero, and 3 CO_2 volume mixing ratio values of 0.9, 0.95, and 1.0.

Fig. 19

Table 11

Figures 19 shows comparison of global mean radiative fluxes, flux convergences, and temperature tendencies for the 500 hPa moist atmosphere between the line-by-line calculation and k-distribution calculations with the generated table. Global mean of solar radiation flux is calculated in the same manner as in Section 4.2. Incident solar radiation flux, its spectrum, and surface albedo are the same as those described in Section 5.1b. The results of the k-distribution calculation are very close to those of the line-by-line calculation. The RMSEs in this case are smaller than the values of target accuracy set in this study (Table 11).

Finally, by the use of the generated table, it is checked that the radiative fluxes and temperature tendencies by the k-distribution calculations are within the range of those by other models in the conditions of Sections 5.1a and 5.1b. The results of those comparisons are shown in supplementary materials. These results indicate that the developed correlated k-distribution model for Mars reproduces the results of the line-by-line model for atmospheres with a wide surface pressure range.

5.3 Radiative-convective equilibrium

As is the case for the Venus, the equilibrium structures of the atmosphere are obtained by the use of a simple one dimensional radiative-convective model with the correlated k-distribution model described above. Atmosphere is assumed to be dry in the altitude region where the atmospheric temperature is higher than the condensation temperature of CO_2. The dry convective adjustment is applied when the lapse rate is greater than the dry adiabatic lapse rate. When the atmospheric temperature decreases below the condensation temperature of CO_2, condensation is assumed to occur to keep the temperature to be condensation temperature. It is assumed that the condensate particles fall instantaneously to the underlying unsaturated layer and sublimes there. CO_2 cloud is not considered. The incident solar radiation flux is assumed to be 75% of present value, i.e. 443.5 W m^{-2}. In order to emulate the global mean structure, the method same as that described in Section 4.2 is used. Solar flux spectrum and surface albedo are the same as those described in Section 5.1c. Gravitational acceleration and specific heat at constant pressure are listed in Table 4. The atmospheric surface pressures given in the calculations range from 10^2 Pa to 6×10^5 Pa. This range covers the surface pressure of the present Mars atmosphere to that of atmospheric collapse. Initial atmospheric profile for integration is composed of two or three layers depending on the surface pressure: a dry adiabatic lower layer from the surface with surface temperature of 250 K, a CO_2 saturated middle layer if any, and an isothermal stratosphere of 167 K. The number of layers (levels) used for calculation depends on the surface pressure: 42 layers (43 levels) for cases with surface pressures of 1, 2, 3, 6×10^2 Pa, 48 layers (49 levels) for cases with surface pressures of 1, 2, 3, 6×10^3 Pa, 56 layers (57 levels) for cases with surface pressures of 1, 2, 3, 6×10^4 Pa, and 63 layers (64 levels) for cases with surface pressures of 1, 2, 3, 6×10^5 Pa. For all cases, the layer thickness is set to 0.2 scale height.

Figure 20 shows the temperature profiles when the model atmospheres are regarded to reach their equilibrium states. CO_2 condensation temperature and a line of 273.15 K are also shown for comparison. Atmospheric temperature decreases with increasing altitude up to about 10 Pa level, but it increases with increasing altitude above the level. This temperature increase in middle atmosphere is caused by absorption of solar near infrared radiation. In cases with surface pressure larger than 2×10^4 Pa, CO_2 condenses in the atmosphere as shown by previous studies (e.g., Kasting 1991). Figure 21 shows dependence of surface temperature on surface pressure. This result compares well with those by previous studies (e.g., Wordsworth et al. 2010; Ramirez et al. 2014). Surface temperature increases with increasing surface pressure up to 2×10^5 Pa, but it decreases above that due to Rayleigh scattering (e.g., Kasting 1991). The effect of Rayleigh scattering can be seen in temperature profiles shown in Fig. 20. Temperature whose black body radiation is equal to the outgoing planetary radiation for each profile is also plotted as cross markers in the figure. The black body temperature decreases with increasing surface pressure. As a result, the surface temperature remains far below 273.15 K for all cases in the range of given surface pressure, as argued by the previous studies.

Fig. 20

Fig. 21

6. Conclusions

In this paper, a set of a line-by-line and a correlated *k*-distribution radiation models which are applicable to various planetary atmospheres have been presented. With the combination of these two radiation models, both an accurate estimate of radiation spectra and a rapid and qualified calculation of radiation field can be ensured. Sequences of procedures to generate radiation parameters for the models, to calculate radiation fields by the models, and to verify those results have been demonstrated.

The developed line-by-line model has been validated by comparing results with available observations and results of other models under conditions of Venus, and present and possible early Mars. The radiation fields calculated by our model agree well with the observed values and are within the scattered ranges of those of other preceding models. This means that the model is applicable, by synthesizing the spectral properties in the same manner as presented here, to a wide range of conditions on various planets.

Then, the common procedure for correlated *k*-distribution models for Venus and Mars have been developed based on optical properties calculated by the line-by-line model. The *k*-distribution tables have been generated with the evaluation of errors which are generated when the numbers of bands and integration points in each band are decreased and when the interpolations of *k*-distribution tables are used. We have proposed, for our Venus and Mars settings, the numbers of bands and integration points, and grid intervals of tables which produce the radiation fields with no significant errors and actually within the uncertainty of the previous models. The proposed numbers of bands and integration points for Venus are 26 and 171, respectively, and are not significantly different from those by a previous study, e.g., 28 bands and total 224 points, respectively (Ikeda 2010). Those for Mars are 20 and 250, respectively, and are not significantly different from those by the previous study, e.g., 14 bands and total 448 points, respectively (Mischna et al. 2012). We confirmed that these numbers of bands and integration points determined by applying our procedure are uniformly applicable for calculating the radiation fields of various planetary atmospheres in the vast parameter space ranging from the present Mars to Venus. The number of bands can be reduced according to the simplicity of the atmospheric components. This is the reason that the number of bands can be smaller for Mars than for Venus. Depending on the problems to be concerned, there may be a room for further optimization for these values. However, we can at least guarantee that the errors increase significantly if the numbers of bands and integration points are halved or grid intervals of tables are doubled from those presented in our work.

By the use of the developed correlated k-distribution models for Venus and Mars, the radiation field of Venus has been evaluated, and the one-dimensional radiative-convective equilibrium profiles for Venus and Mars have been calculated. The evaluated radiation field of Venus compares well with observations and those presented by previous studies, although evaluation here assumes horizontally uniform distributions of the composition and the cloud. The radiative-convective equilibrium calculation for Venus shows a thermal structure with a neutral layer corresponding to the cloud layer which is observed in Venus atmosphere. It has also been shown that stability in the Venus lower atmosphere is stable and the value is sensitive to the amount of water vapor. The radiative-convective equilibrium calculation for Mars has shown that surface pressure dependence of surface temperature agrees well with those reported by previous studies. These are the applications that demonstrate the validity and usefulness of our correlated k-distribution models developed in this study. Especially, the systematic generation of k-distribution tables and interpolation method work fairly well. The procedure presented here is vital in parameter study of planetary atmospheres.

This paper has provided detailed descriptions on our line-by-line model and our correlated k-distribution model. Radiation fields in various planetary atmospheres can be investigated by the use of these models. One of the examples of application is implementation of the correlated k-distribution models into GCMs. We are now carrying out researches in this direction. If the computational cost for radiation calculation has to be decreased further in the course of implementation into GCMs, the numbers of bands and integration points are decreased at the expense of accuracy with reference to the numbers determined in this study as standards. The models developed in this study will be important basic tools to perform researches on climates of planets in our solar system and plausible exoplanets.

Appendix A. Line cutoff function

Line cutoff function depends on species. As for CO_2 lines, sub-Lorentzian factor of Perrin and Hartmann (1989) is used. As for other species' lines, the following function is used:

$$\chi(\nu, \nu_{c,m,i}, \Delta\nu_m) = \begin{cases} 1 - \left(\dfrac{\nu - \nu_{c,m,i}}{\Delta\nu_m}\right)^2 & (|\nu - \nu_{c,m,i}| \leq \Delta\nu_m) \\ 0 & (|\nu - \nu_{c,m,i}| > \Delta\nu_m) \end{cases}, \tag{A.1}$$

where ν is wavenumber, $\nu_{c,m,i}$ is wavenumber at the center of ith line of mth molecular species and $\Delta\nu_m$ is cutoff wavenumber of mth molecular species. This function is selected because the use of this factor results in better agreement in absorption coefficients with calculations by LBLRTM (Clough et al. 2005).

Appendix B. Band average of optical properties of particles

Rayleigh scattering coefficients and optical properties of particle species at ith band are obtained by averaging the line-by-line values over wavenumber in each band, as follows:

$$\overline{k}_{Rs,i} = \frac{\int_{\Delta\nu_i} F(\nu) k_{Rs}(\nu) d\nu}{\int_{\Delta\nu_i} F(\nu) d\nu}, \tag{B.2}$$

$$\overline{Q}_{e,i} = \frac{\int_{\Delta\nu_i} F(\nu) Q_e(\nu) d\nu}{\int_{\Delta\nu_i} F(\nu) d\nu}, \tag{B.3}$$

$$\overline{\varpi}_{0,i} = \frac{\int_{\Delta\nu_i} F(\nu) Q_e(\nu) \varpi_0(\nu) d\nu}{\int_{\Delta\nu_i} F(\nu) Q_e(\nu) d\nu}, \tag{B.4}$$

$$\overline{g}_i = \frac{\int_{\Delta\nu_i} F(\nu) Q_e(\nu) \varpi_0(\nu) g(\nu) d\nu}{\int_{\Delta\nu_i} F(\nu) Q_e(\nu) \varpi_0(\nu) d\nu}, \tag{B.5}$$

where $\Delta\nu_i$, F, k_{Rs}, Q_e, ϖ_0, g are wavenumber width of ith band, sum of the Planck function and the solar flux, Rayleigh scattering coefficient, extinction efficiency factor, single scattering albedo, and asymmetry factor, respectively. In developing correlated k-distribution models for Venus and

Mars in this study, the Planck function at 250 K and an incident solar flux at the distance of semi-major axis from the Sun are used in calculating band average values. It may be worth notifying that the radiative fields calculated by the correlated *k*-distribution for Venus and Mars are not sensitive to the assumed temperature of 250 K, and the conclusion on the comparisons does not change even if the temperature is changed.

Data availability

The data generated and analyzed in this study will be available at the JMSJ's J-STAGE Data site, except for those already published elsewhere. Software developed and used in this study and its newest versions will be available from the web page of GFD Dennou Club, `https://www.gfd-dennou.org/`.

Acknowledgements

The authors would like to thank Michael A. Mischna for providing us data of radiative fluxes and temperature tendencies shown in his paper. We are also grateful to two anonymous reviewers for their constructive comments on this article. Visualization software developed by GFD Dennou Club, Dennou Club Library (DCL) and GPhys, are used to make plots shown in this study. A supercomputer of the Education Center on Computational Science and Engineering, Kobe University is used to perform several calculations shown in this study. This study was funded by Grant-in-Aid for Scientific Research on Innovative Areas (JSPS KAKENHI Grant Numbers 17H06457 and 19H05605) from Japan Society for the Promotion of Science.

References

Allen, D. A., and J. W. Crawford, 1984: Cloud structure on the dark side of venus. *Nature*, **307**, 222–224.

Ando, H., T. Imamura, S. Tellmann, M. Patzold, B. Hausler, N. Sugimoto, M. Takagi, H. Sagawa, S. Limaye, Y. Matsuda, R. K. Choudhary, and M. Antonita, 2020: Thermal structure of the venusian atmosphere from the sub-cloud region to the mesosphere as observed by radio occultation. *Sci. Rep.*, **10**, 3448.

Baranov, Y. I., W. J. Lafferty, and G. T. Fraser, 2004: Infrared spectrum of the continuum and dimer absorption in the vicinity of the o_2 vibrational fundamental in o_2/co_2 mixtures. *J. Mol. Spectrosc.*, **228**, 432–440.

Bézard, B., C. de Bergh, D. Crisp, and J.-P. Maillard, 1990: The deep atmosphere of venus revealed by high-resolution nightside spectra. *Nature*, **345**, 508–511.

Bézard, B., A. Fedorova, J.-L. Bertaux, A. Rodin, and O. Korablev, 2011: The 1.10- and 1.18-μm nightside windows of venus observed by spicav-ir aboard venus express. *Icarus*, **216**, 173–183.

Clough, S. A., M. W. Shephard, E. J. Mlawer, J. S. Delamere, M. J. Iacono, K. Cady-Pereira, S. Boukabara, and P. D. Brown, 2005: Atmospheric radiative transfer modeling: a summary of the aer codes. *J. Quant. Spectrosc. Radiat. Transfer*, **91**, 233–244.

Crisp, D., 1986: Radiative forcing of the venus mesosphere i. solar fluxes and heating rates. *Icarus*, **67**, 484–514.

Crisp, D., 1989: Radiative forcing of the venus mesosphere ii. thermal fluxes, cooling rates, and radiative equilibrium temperatures. *Icarus*, **77**, 391–413.

Eymet, V., C. Coustet, and B. Piaud, 2016: kspectrum: an open-source code for high-resolution molecular absorption spectra production. *J. Phys. Conf. Ser.*, **676**, 012005.

Eymet, V., R. Fournier, J.-L. Dufresne, S. Lebonnois, F. Hourdin, and M. A. Bullock, 2009: Net exchange parameterization of thermal infrared radiative transfer in venus' atmosphere. *J. Geophys. Res.*, **114**, E11008.

Fedorova, A., O. Korablev, A.-C. Vandaele, J.-L. Bertaux, D. Belyaev, A. Mahieux, E. Neefs, W. V. Wilquet, R. Drummond, F. Montmessin, and E. Villard, 2008: Hdo and h2o vertical distributions and isotopic ratio in the venus mesosphere by solar occultation at infrared spectrometer on board venus express. *J. Geophys. Res.*, **113**, E00B22.

Freeman, D. E., K. Yoshino, J. R. Esmond, and W. H. Parkinson, 1984: High resolution absorption cross section measurements of so_2 at 213 k in the wavelength region 172–240 nm. *Planetary and Space Science*, **32**, 1125–1134.

Golovin, Y. M., B. Y. Moshkin, and A. P. Ekonomov, 1983: Some optical properties of the venus surface. *Venus*, D. M. Hunten, L. Colin, T. M. Donahue and V. I. Moroz, Eds., The University of Arizona Press, Tucson, Arizona chapter 7, 131–136.

Gruszka, M., and A. Borysow, 1997: Roto-translational collision-induced absorption of co_2 for the atmosphere of venus at frequencies from 0 to 250 cm -1, at temperatures from 200 to 800 k. *Icarus*, **129**, 172–177.

Gueymard, C. A., 2004: The sun's total and spectral irradiance for solar energy applications and solar radiation models. *Solar Energy*, **76**, 423–453.

Haberle, R. M., M. A. Kahre, J. L. Hollingsworth, F. Montmessin, R. J. Wilson, R. A. Urata, A. S. Brecht, M. J. Wolff, A. M. Kling, and J. R. Schaeffer, 2019: Documentation of the nasa/ames legacy mars global climate model: Simulations of the present seasonal water cycle. *Icarus*, **333**, 130–164.

Hansen, J. E., and L. D. Travis, 1974: Light scattering in planetary atmospheres. *Space Sci. Rev.*, **16**, 527–610.

Haqq-Misra, J. D., S. D. Domagal-Goldman, P. J. Kasting, and J. F. Kasting, 2008: A revised hazy methane greenhouse for the archean earth. *Astrobiology*, **8**, 1127–1137.

Haus, R., D. Kappel, and G. Arnold, 2013: Self-consistent retrieval of temperature profiles and cloud structure in the northern hemisphere of venus using virtis/vex and pmv/venera-15 radiation measurements. *Planet. Space Sci.*, **89**, 77–101.

Haus, R., D. Kappel, and G. Arnold, 2015: Radiative heating and cooling in the middle and lower atmosphere of venus and responses to atmospheric and spectroscopic parameter variations. *Planet. Space Sci.*, **117**, 262–294.

Hermansa, C., A. C. Vandaele, and S. Fally, 2009: Fourier transform measurements of so_2 absorption cross sections:: I. temperature dependence in the 24000–29000 cm^{-1} (345–420 nm) region. *J. Quant. Spectrosc. Radiat. Transfer*, **110**, 756–765.

Hourdin, F., 1992: A new representation of the absorption by the co_2 15-μm band for a martian general circulation model. *J. Geophys. Res.*, **97**, 18,319–18,335.

Ikeda, K., 2010: , *Development of radiative transfer model for Venus atmosphere and simulation of superrotation using a general circulation model*. PhD thesis, U. Tokyo.

Irwin, P. G. J., N. A. Teanby, R. de Kok, L. N. Fletcher, C. J. A. Howett, C. F. W. C. C. C. Tsang, S. B. Calcutt, C. A. Nixon, and P. D. Parrish, 2008: The nemesis planetary atmosphere radiative transfer and retrieval tool. *J. Quant. Spectrosc. Radiat. Transfer*, **109**, 1136–1150.

Ito, Y., G. L. Hashimoto, Y. O. Takahashi, M. Ishiwatari, and K. Kuramoto, 2020: H_2o_2-induced greenhouse warming on oxidized early mars. *The Astrophysical Journal*, **893(2)**, 168.

Kasting, J. F., 1991: Co_2 condensation and the climate of early mars. *Icarus*, **94**, 1–13.

Kylling, A., and K. Stamnes, 1995: A reliable and efficient two-stream algorithm for spherical radiative transfer: Documentation of accuracy in realistic layered media. *J. Atmos. Chem.*, **21**, 115–150.

Lebonnois, S., V. Eymet, C. Lee, and J. V. d'Ollone, 2015: Analysis of the radiative budget of the venusian atmosphere based on infrared net exchange rate formalism. *J. Geophys. Res.*, **120**, 1186–1200.

Lebonnois, S., F. Hourdin, V. Eymet, A. Crespin, R. Fournier, and F. Forget, 2010: Superrotation of venus' atmosphere analyzed with a full general circulation model. *J. Geophys. Res.*, **115**, E06006.

Lebonnois, S., G. Schubert, F. Forget, and A. Spiga, 2018: Planetary boundary layer and slope winds on venus. *Icarus*, **314**, 149–158.

Lee, C., and M. I. Richardson, 2011: A discrete ordinate, multiple scattering, radiative transfer model of the venus atmosphere from 0.1 to 260 mm. *J. Atmos. Sci.*, **68**, 1323–1339.

Lee, Y. J., H. Sagawa, R. Haus, S. Stefani, T. Imamura, D. V. Titov, and G. Piccioni, 2016: Sensitivity of net thermal flux to the abundance of trace gases in the lower atmosphere of venus. *J. Geophys. Res.*, **121**, 1737–1752.

Marcq, E., T. Encrenaz, B. Bezard, and M. Birlan, 2006: Remote sensing of venus' lower atmosphere from ground-based ir spectroscopy: Latitudinal and vertical distribution of minor species. *Planet. Space Sci.*, **54**, 1360–1370.

Marov, M. Y., V. S. Avduevsky, N. F. Borodin, A. P. Ekonomov, V. V. Kerzhanovich, V. P. Lysov, B. Y. Moshkin, M. K. Rozhdestvensky, and O. L. Ryabov, 1973: Preliminary results on the ven us atmosphere from the venera 8 descent module. *Phil. Trans. R. Soc. A*, **20**, 407–421.

Meadows, W. E., and W. R. Weaver, 1980: Two-stream approximations to radiative transfer in planetary atmospheres: A unified description of existing methods and a new improvement. *J. Atmos. Sci.*, **37**, 630–643.

Mendonça, J. M., P. L. Read, C. F. Wilson, and C. Lee, 2015: A new, fast and flexible radiative transfer method for venus general circulation models. *Planet. Space Sci.*, **105**, 80–93.

Mischna, M. A., C. Lee, and M. Richardson, 2012: Development of a fast, accurate radiative transfer model for the martian atmosphere, past and present. *J. Geophys. Res.*, **117**, E10009.

Mlawer, E. J., V. H. Payne, J.-L. Moncet, J. S. Delamere, M. J. Alvarado, and D. C. Tobin, 2012: Development and recent evaluation of the mt_ckd model of continuum absorption. *Phil. Trans. R. Soc. A*, **370**, 2520–2556.

Mlawer, E. J., S. J. Taubman, P. D. Brown, M. J. Iacono, and S. A. Clough, 1997: Radiative transfer for inhomogeneous atmospheres: RRTM, a validated correlated-k model for the longwave. *J. Geophys. Res.*, **102**, 16663–16682.

Moroz, V. I., A. P. Ekonomov, B. E. Moshkin, H. E. Revercomb, L. A. Sromovsky, J. T. Schofield, D. Spänkuch, F. W. Taylor, and M. G. Tomasko, 1985: Solar and thermal radiation in the venus atmosphere. *Adv. Space Res.*, **5**, 197–232.

Pavlov, A. A., J. F. Kasting, L. L. Brown, K. A. Rages, and R. Freedman, 2000: Greenhouse warming by ch4 in the atmosphere of early earth. *J. Geophys. Res.*, **105**, 11,981–11,990.

Perrin, M. Y., and J. M. Hartmann, 1989: Temperature-dependent measurements and modeling of absorption by $\mathrm{co_2}$-$\mathrm{n_2}$ mixtures in the far line-wings of the 4.3 μm $\mathrm{co_2}$ band. *J. Quant. Spectrosc. Radiat. Transfer*, **42**, 311–317.

Pierrehumbert, R. T., 2010: *Principles of Planetary Climate.* Cambridge University Press.

Pollack, J. B., J. B. Dalton, D. Grinspoon, R. B. Wattson, R. Freedman, D. Crisp, D. A. Allen, B. Bezard, C. DeBergh, L. P. Giver, Q. Ma, and R. Tipping, 1993: Near-infrared light from venus nightside: A spectroscopic analysis. *Icarus*, **103**, 1–42.

Ramirez, R. M., R. Kopparapu, M. E. Zugger, T. D. Robinson, R. Freedman, and J. F. Kasting, 2014: Warming early mars with $\mathrm{co_2}$ and $\mathrm{h_2}$. *Nature Geosci.*, **7**, 59–63.

Read, P. L., J. Barstow, B. Charnay, S. Chelvaniththilan, P. G. J. Irwin, S. Knight, S. Lebonnois, S. R. Lewis, J. Mendonça, and L. Montaboneb, 2016: Global energy budgets and 'trenberth diagrams' for the climates of terrestrial and gas giant planets. *Q. J. R. Meteorol. Soc.*, **142**, 703–720.

Revercomb, H. E., L. A. Sromovsky, V. E. Suomi, and R. W. Boese, 1985: Net thermal radiation in the atmosphere of venus. *Icarus*, **61**, 521–538.

Richard, C., I. E. Gordon, M. A. L. S. Rothman and, L. Frommhold, M. Gustafsson, J.-M. Hartmann, C. Hermans, W. J. Lafferty, G. S. Orton, K. M. Smith, and H. Tran, 2012: New section of the hitran database: Collision-induced absorption (cia). *J. Quant. Spectrosc. Radiat. Transfer*, **113**, 1276–1285.

Rothman, L. S., I. E. Gordon, Y. Babikov, A. Barbe, D. ChrisBenner, P. F. Bernath, M. Birk, L. Bizzocchi, V. Boudon, L. R. Brown, A. Campargue, K. Chance, E. A. Cohen, L. H. Coudert, V. M. Devi, B. J. Drouin, A. Fayt, J.-M. Flaud, R. R. Gamache, J. J. Harrison, J.-M. Hartmann, C. Hill, J. T. Hodges, D. Jacquemart, A. Jolly, J. Lamouroux, R. J. LeRoy, G. Li, D. A. Long, O. M. Lyulin, C. J. Mackie, S. T. Massie, S. Mikhailenko, H. S. P. Muller, O. V. Naumenko, A. V. Nikitin, J. Orphal, V. Perevalov, A. Perrin, E. R. Polovtseva, C. Richard, M. A. H. Smith, E. Starikova, K. Sung, S. Tashkun, J. Tennyson, G. C. Toon, V. G. Tyuterev, and G. Wagner, 2013: The hitran2012 molecular spectroscopic database. *J. Quant. Spectrosc. Radiat. Transfer*, **130**, 4–50.

Rothman, L. S., I. E. Gordon, R. J. Barber, H. Dothe, R. R. Gamache, A. Goldman, V. I. Perevalov, S. A. Tashkun, and J. Tennyson, 2010: Hitemp, the high-temperature molecular spectroscopic database. *J. Quant. Spectrosc. Radiat. Transfer*, **111**, 2139–2150.

Schofield, J. T., and F. W. Taylor, 1982: Net global thermal emission from the venusian atmosphere. *Icarus*, **52**, 245–262.

Schubert, G., 1983: General circulation and the dynamical state of the venus atmosphere. *Venus*, D. M. Hunten, L. Colin, T. M. Donahue and V. I. Moroz, Eds., The University of Arizona Press, Tucson, Arizona chapter 21, 681–765.

Seiff, A., D. B. Kirk, R. E. Young, R. C. Blanchard, J. T. Findlay, G. M. Kelly, and S. C. Sommer, 1980: Measurements of thermal structure and thermal contrasts in the atmosphere of venus and related dynamical observations: Results from the four pioneer venus probes. *J. Geophys. Res.*, **85**, 7903–7933.

Seiff, A., J. T. Schofield, A. J. Kliore, F. W. Taylor, S. S. Limaye, H. E. Revercomb, L. A. Sromovsky, V. V. Kerzhanovich, V. I. Moroz, and M. Y. Marov, 1985: Models of the structure of the atmosphere of venus from the surface to 100 kilometers altitude. *Adv. Space Res.*, **5**, 3.

Stefani, S., G. Piccioni, M. Snels, D. Grassi, and A. Adriani, 2013: Experimental co2 absorption coefficients at high pressure and high temperature. *J. Quant. Spectrosc. Radiat. Transfer*, **117**, 21–28.

Taylor, F. W., D. M. Hunten, and L. V. Ksanfomaliti, 1983: The thermal balance of the middle and upper atmosphere of venus. *Venus*, D. M. Hunten, L. Colin, T. M. Donahue and V. I. Moroz, Eds., The University of Arizona Press, Tucson, Arizona chapter 20, 650–680.

Titov, D. V., M. Bullock, D. Crisp, N. Renno, F. Taylor, and L. Zasova, 2007: Volume 176 of *AGU Geophysical Monograph*, chapter Radiation in the Atmosphere of Venus, 121–138.

Tomasko, M. G., L. R. Doose, P. H. Smith, and A. P. Odell, 1980a: Measurements of the flux of sunlight in the atmosphere of venus. *J. Geophys. Res.*, **85**, 8167–8186.

Tomasko, M. G., P. H. Smith, V. E. Suomi, L. R. Sromovsky, H. E. Revercomb, F. W. Taylor, D. J. Martonchik, A. Seiff, R. Boese, J. B. Pollack, A. P. Ingersoll, G. Schubert, and C. C. Covey, 1980b: The thermal balance of venus in light of the pioneer venus mission. *J. Geophys. Res.*, **85**, 8187–8199.

Toon, O. B., C. P. McKay, T. P. Ackerman, and K. Santhanam, 1989: Rapid calculation of radiative heating rates and photodissociation rates in inhomogeneous multiple scattering atmospheres. *J. Geophys. Res.*, **94**, 16287–16301.

Turbet, M., E. Bolmont, J. Leconte, F. Forget, F. Selsis, G. Tobie, A. Caldas, J. Naar, and M. Gillon, 2018: Modeling climate diversity, tidal dynamics and the fate of volatiles on trappist-1 planets. *Astron. Astrophys.*, **612**, A86.

Wordsworth, R., F. Forget, and V. Eymet, 2010: Infrared collision-induced and far-line absorption in dense co_2 atmospheres. *Icarus*, **210**, 992–997.

Yurchenko, S. N., A. F. Al-Refaie, and J. Tennyson, 2018: Exocross: a general program for generating spectra from molecular line lists. *Astron. Astrophys.*, **614**, A131.

Zasova, L. V., N. Ignatieva, I. Khatuntseva, and V. Linkin, 2007: Structure of the venus atmosphere. *Planet. Space Sci.*, **55**, 1712–1728.

List of Figures

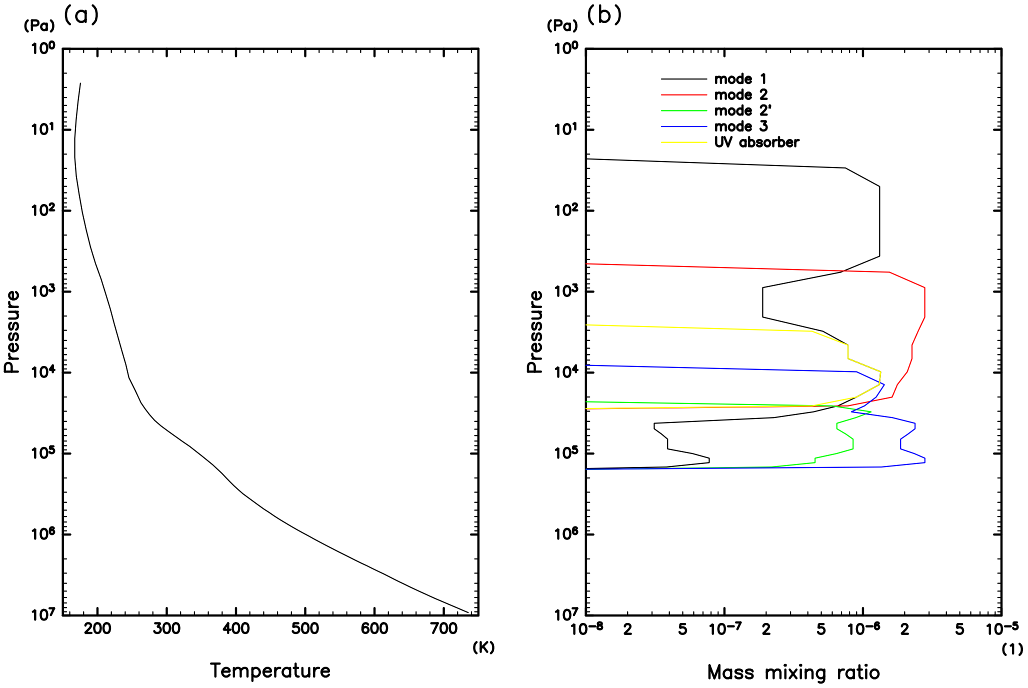

Fig. 1. Vertical profiles used in Venus calculation: (a) temperature and (b) mass mixing ratios of cloud and UV absorber.

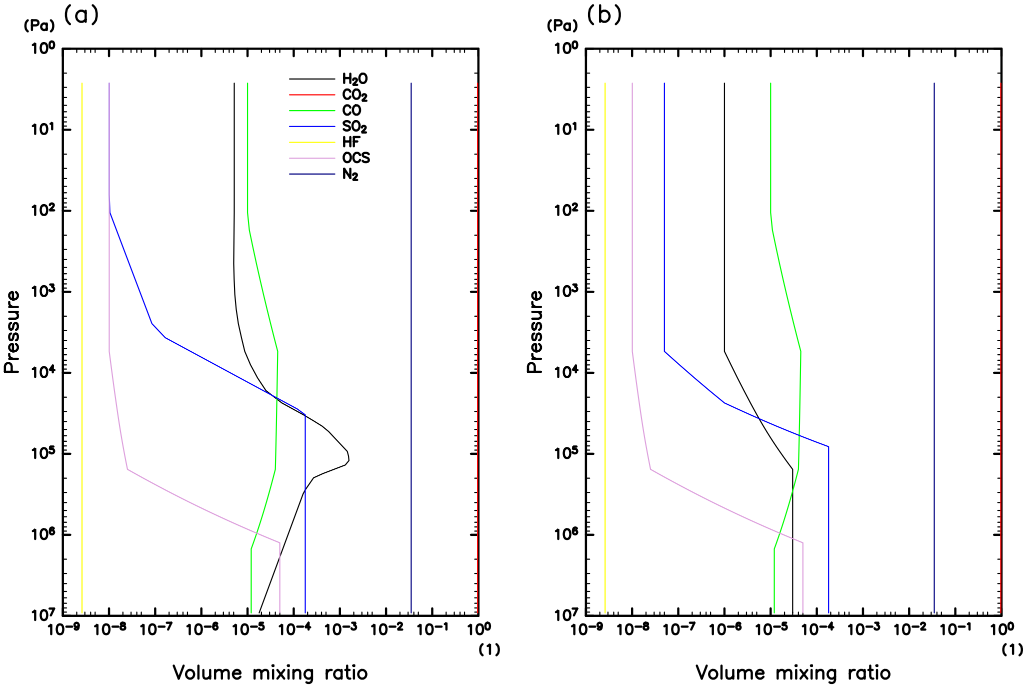

Fig. 2. Vertical profiles used in Venus calculation: gas volume mixing ratios for (a) Case V_A and (b) Case V_B.

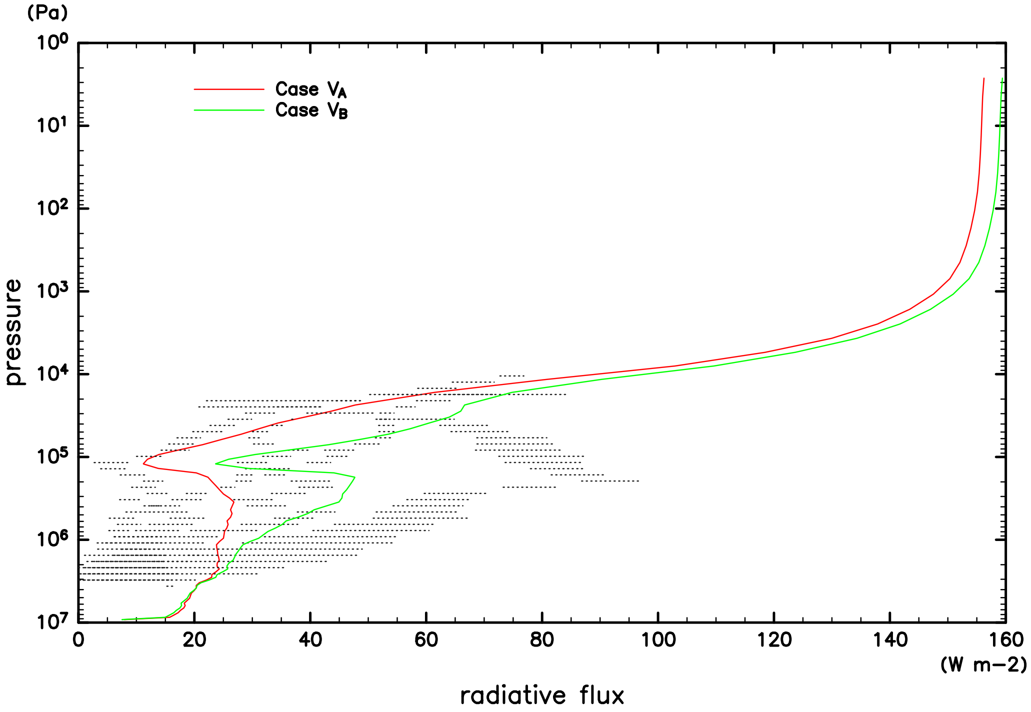

Fig. 3. Longwave net flux profile obtained by the line-by-line calculation for Venus. Red and green lines show fluxes obtained from Cases V_A and V_B, respectively. Hatched regions show net flux observed by the Pioneer Venus probes (Revercomb et al. 1985).

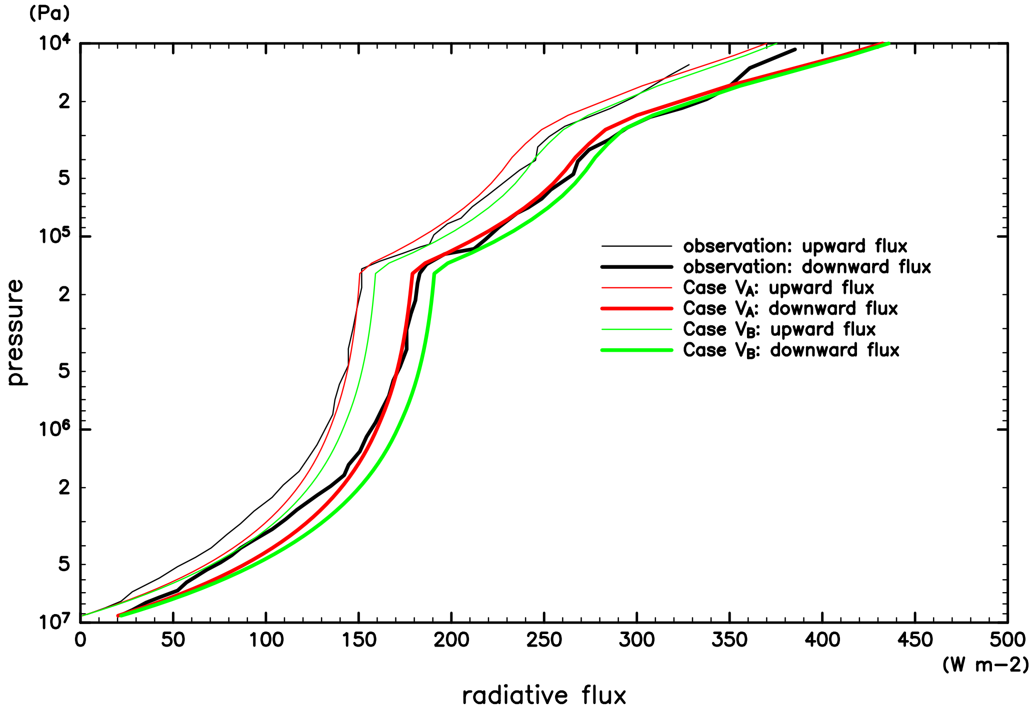

Fig. 4. Upward and downward shortwave (0.4–1.0 μm) radiative flux profiles at the solar zenith angle of 65.6° obtained by the line-by-line calculation for Venus. Red and green lines show profiles obtained from Cases $\mathrm{V_A}$ and $\mathrm{V_B}$, respectively. Black lines show fluxes observed by the Pioneer Venus probe (Tomasko et al. 1980a). Thin and thick lines show upward and downward fluxes, respectively.

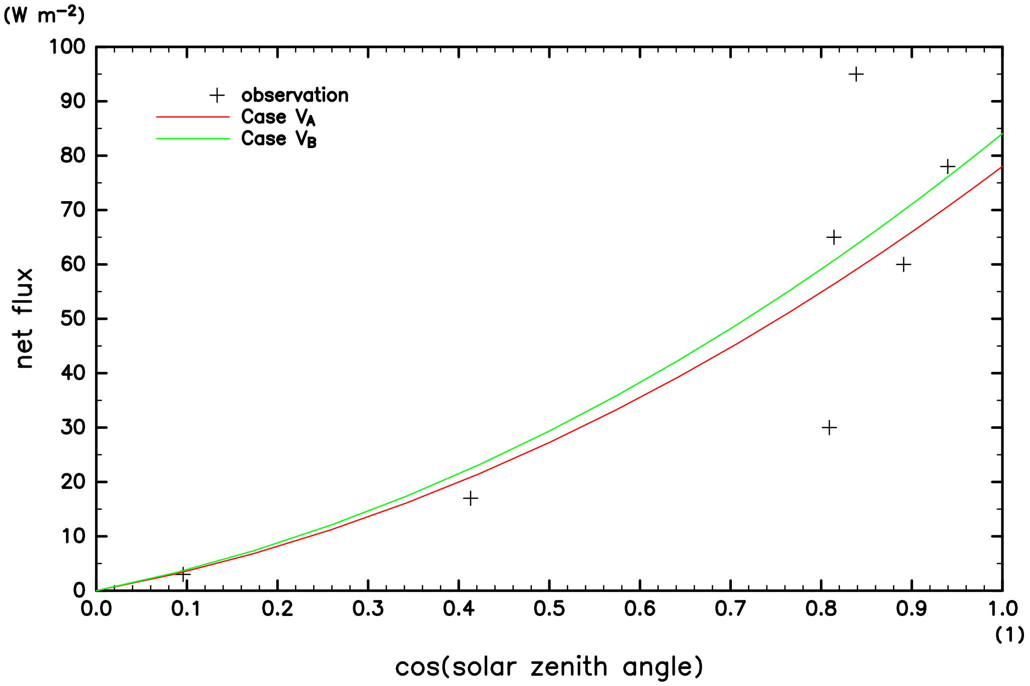

Fig. 5. Solar zenith angle dependence of net shortwave radiative flux at the surface obtained by the line-by-line calculation for Venus. Red and green lines show fluxes obtained from Cases V_A and V_B, respectively. Plus (+) markers show fluxes observed by several missions (Marov et al. 1973; Moroz et al. 1985). It is noted that the downward is positive.

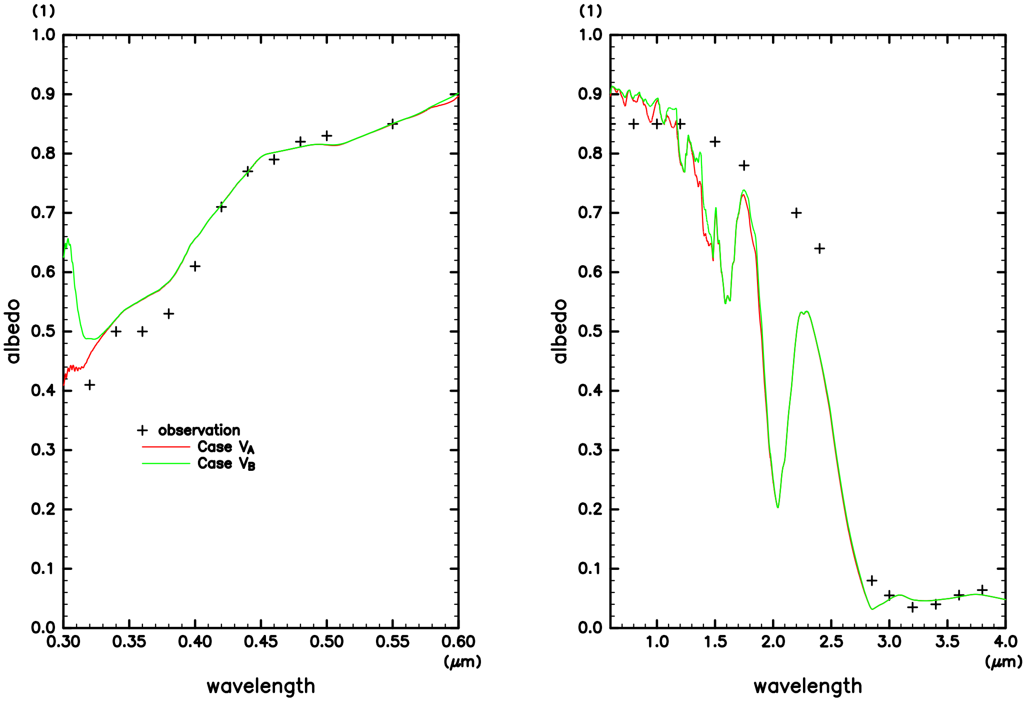

Fig. 6. Wavelength dependence of planetary albedo obtained by the line-by-line calculation for Venus. Red and green lines show albedos obtained from Cases $\mathrm{V_A}$ and $\mathrm{V_B}$, respectively. Running averaged values with 500 cm^{-1} interval are plotted. Plus (+) markers show observed albedo (Moroz et al. 1985).

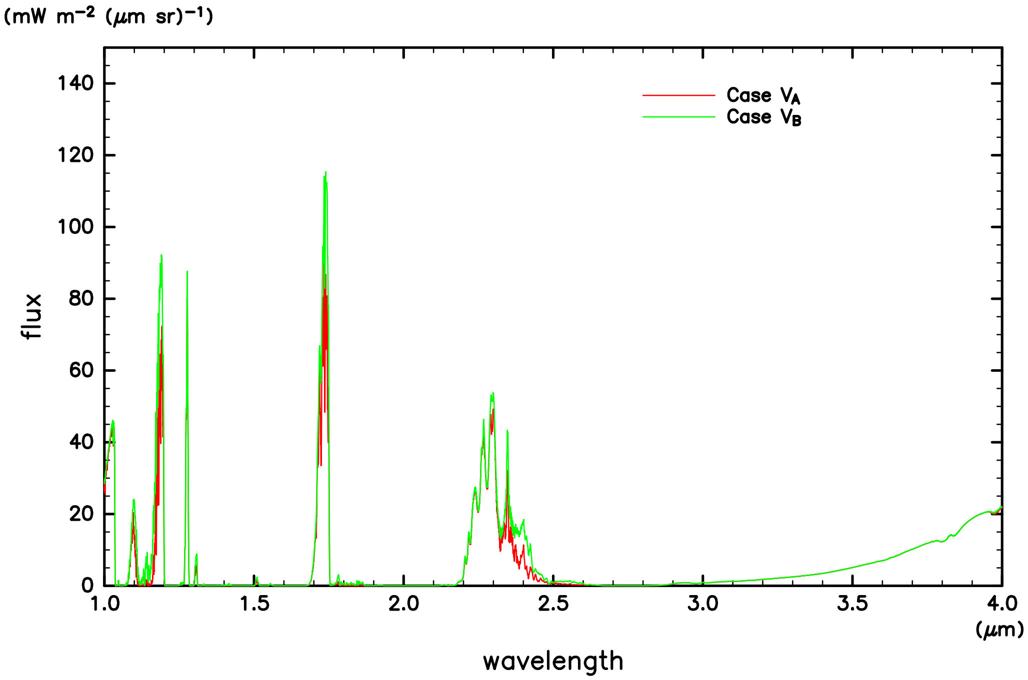

Fig. 7. Nightside near infrared upward radiative flux at the top of the atmosphere obtained by the line-by-line calculation for Venus. Red and green lines show fluxes obtained from Cases V_A and V_B, respectively. Running averaged values with 10 cm^{-1} interval are plotted.

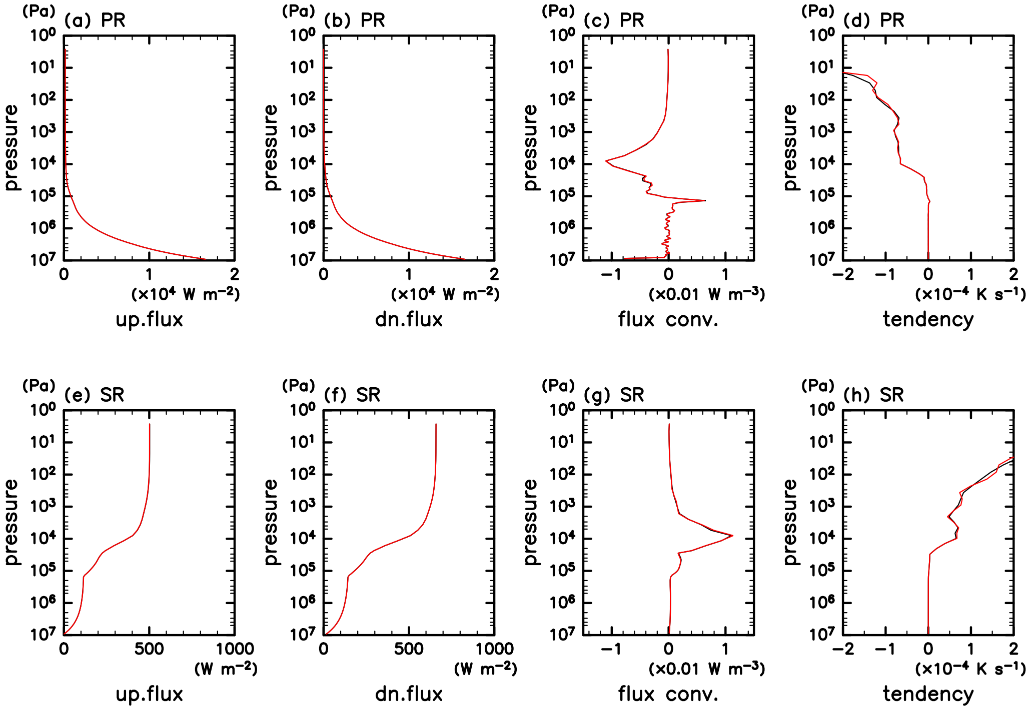

Fig. 8. Upward and downward radiative fluxes (a, e and b, f), flux convergences (c, g), and temperature tendencies (d, h) obtained by the line-by-line calculation (black) and the k-distribution calculation (red) for Venus atmosphere. Panels a–d for planetary radiation and panels e–h for solar radiation.

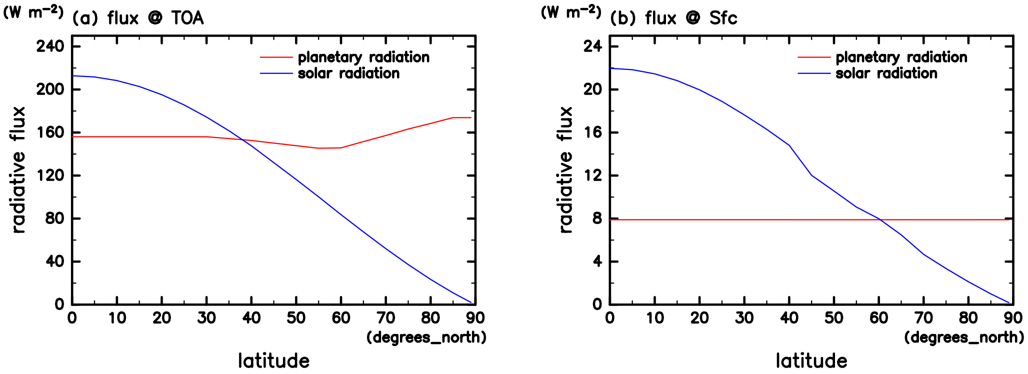

Fig. 9. Meridional distributions of diurnal mean radiative fluxes at the top of the atmosphere (a) and the surface (b) for the VIRA. Red and blue lines show net planetary radiation flux and net solar radiation flux, respectively. Positive is upward for planetary radiation and is downward for solar radiation.

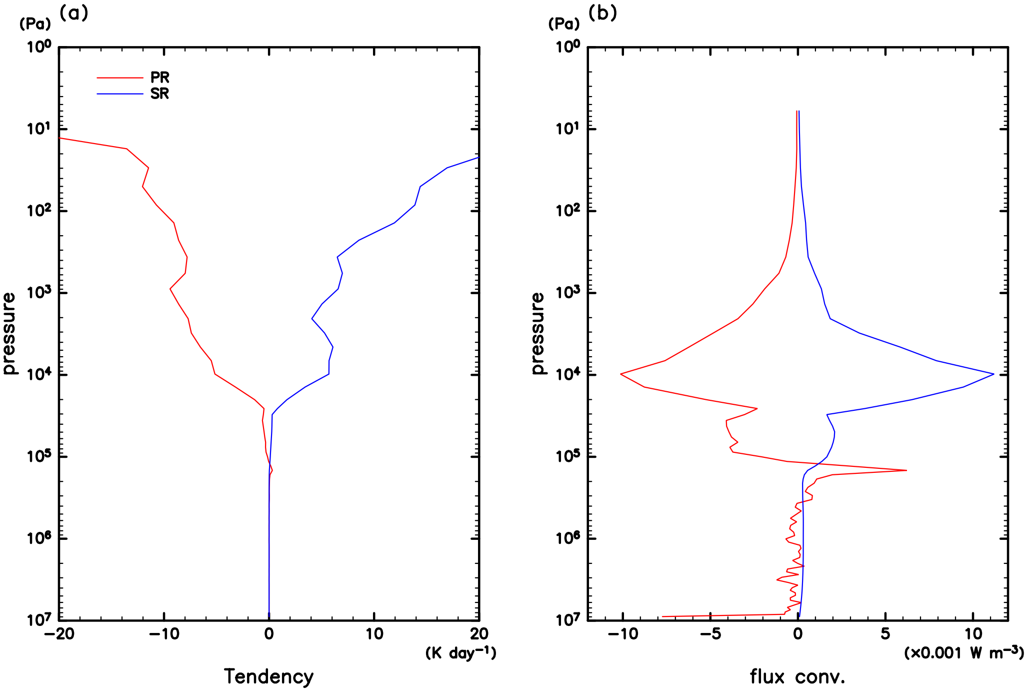

Fig. 10. Global mean temperature tendencies (a) and flux convergences (b) for the VIRA. Red and blue lines show values of planetary radiation and solar radiation heating, respectively.

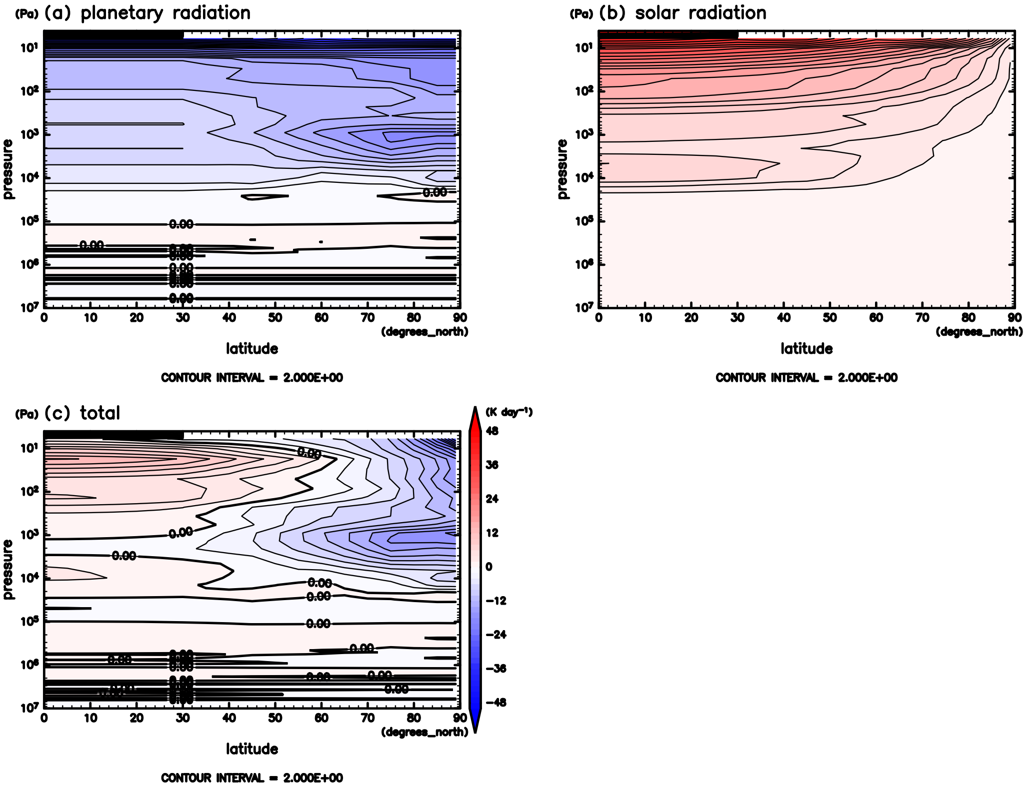

Fig. 11. Meridional distributions of diurnal mean temperature tendency for the VIRA: (a) planetary radiation, (b) solar radiation, and (c) total. Contour interval is 2 K day^{-1}, and thick contour indicates zero.

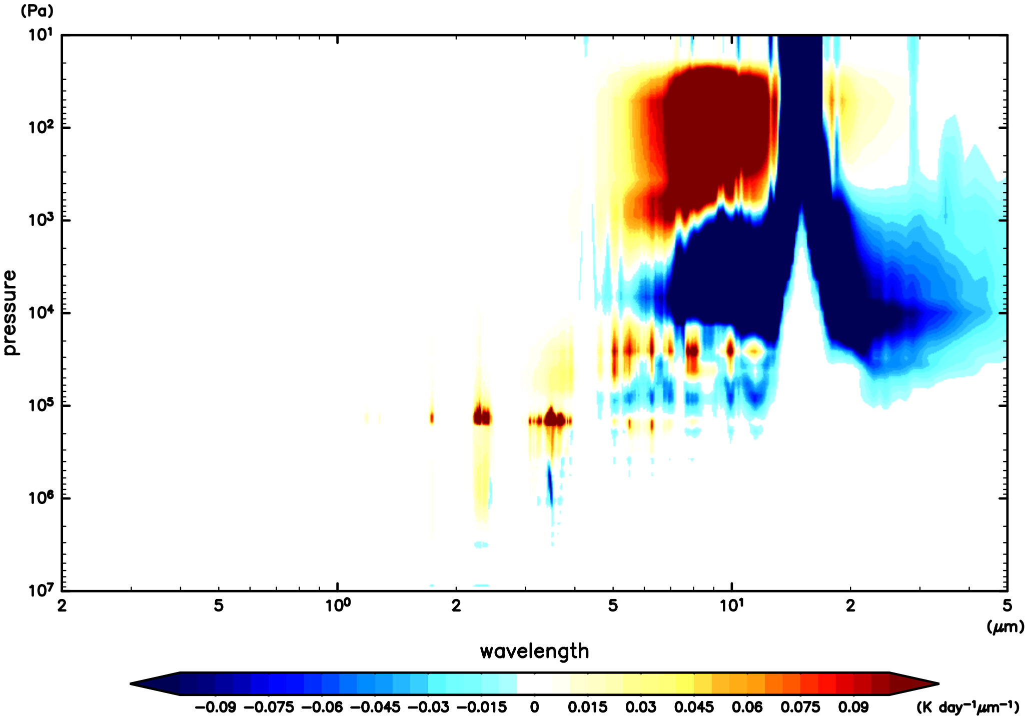

Fig. 12. Planetary radiation temperature tendency spectra as a function of pressure for the low latitude profile of the VIRA. Running averaged values with 15 cm^{-1} interval are plotted.

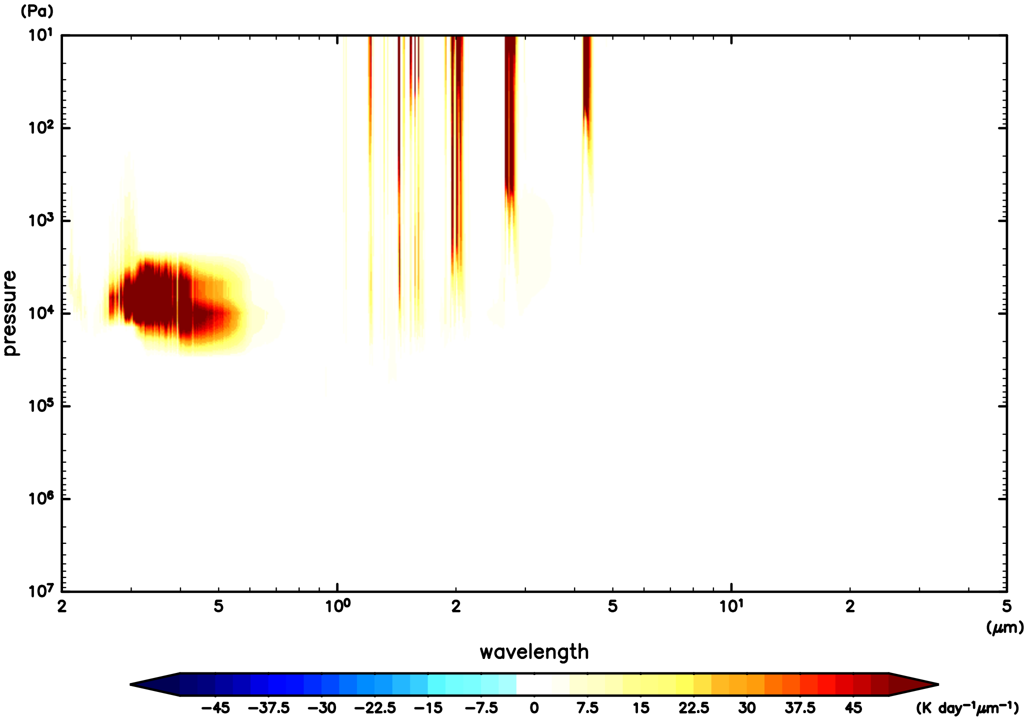

Fig. 13. Same as Fig. 12, but for solar radiation temperature tendency. It should be noticed that the color is different from that of Fig. 12.

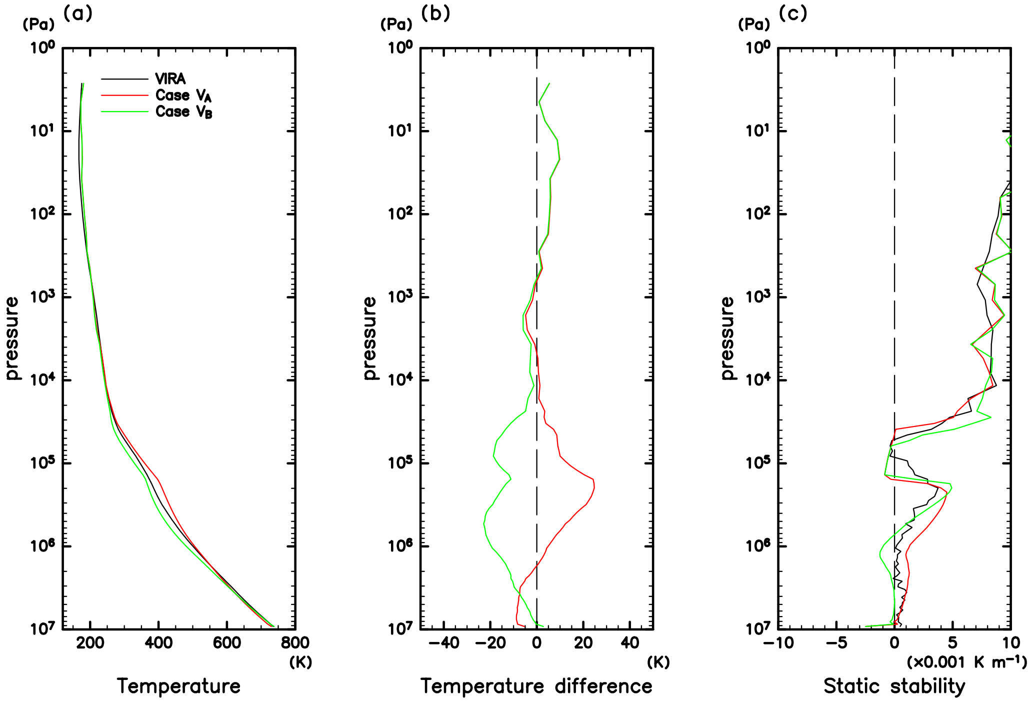

Fig. 14. Radiative-convective equilibrium profiles of Venus: (a) temperature, (b) temperature difference from the low latitude profile of the VIRA, and (c) static stability. Red and green lines show profiles of Cases V_A and V_B, respectively. Black lines show profiles of the VIRA.

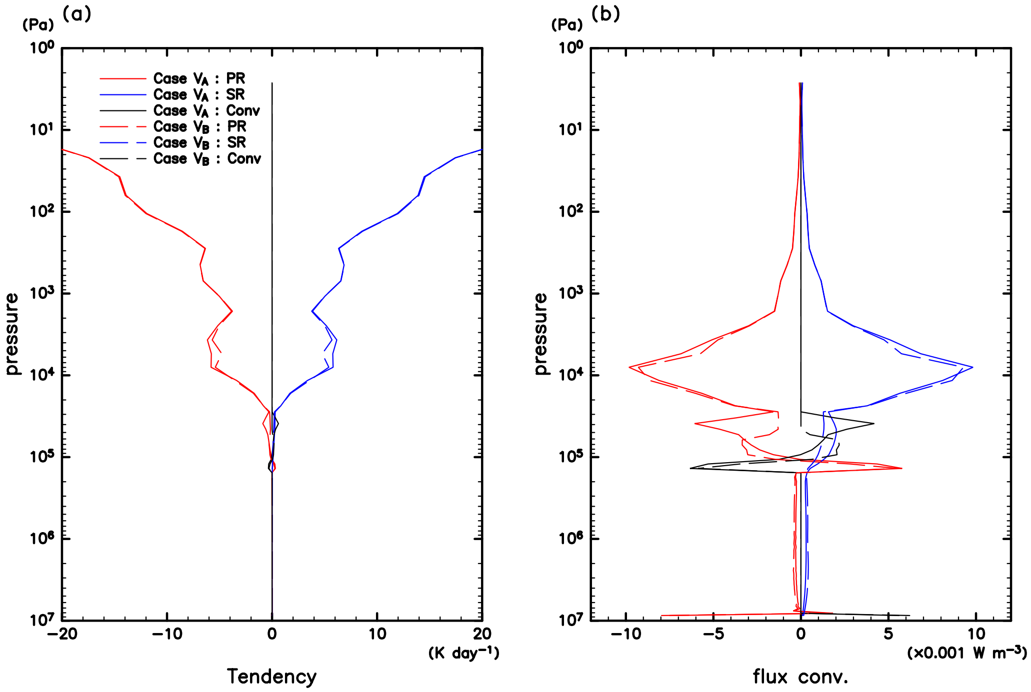

Fig. 15. Temperature tendencies (a) and flux convergences (b) for radiative-convective equilibrium profiles of Venus. Solid and dashed lines show values of Cases V_A and V_B, respectively. Red, blue, and black lines show values of planetary radiation, solar radiation and convective heating, respectively.

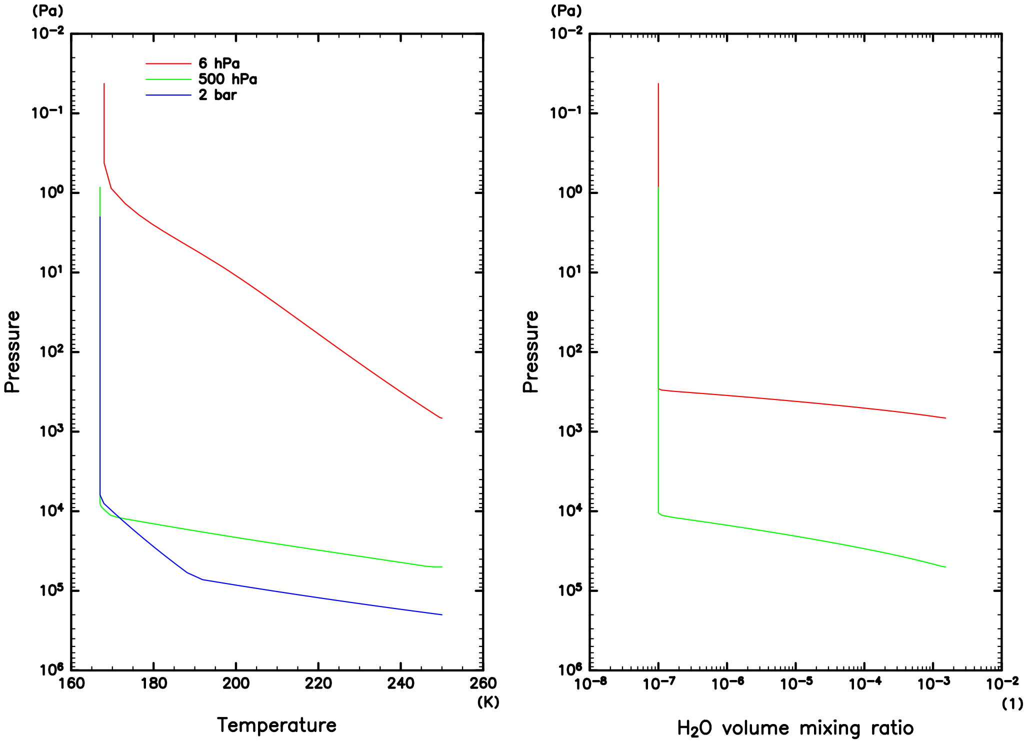

Fig. 16. Vertical profiles of temperature and H_2O volume mixing ratio used in calculations for Mars atmosphere. Red, green, and blue lines show profiles for 6 hPa, 500 hPa, and 2 bar atmospheres, respectively.

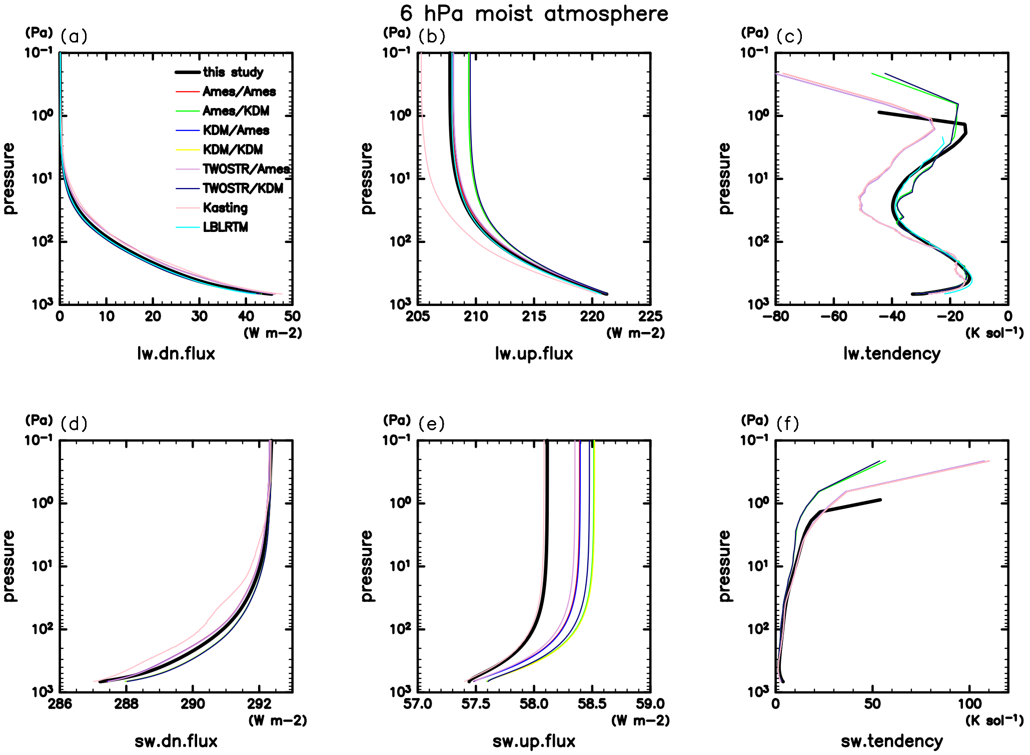

Fig. 17. Upward and downward radiative fluxes and temperature tendencies calculated for the 6 hPa Mars moist atmosphere. Panels a–c show fluxes and temperature tendencies of longwave, and d–f show those of shortwave. Panels a and d show upward fluxes, b and e show downward fluxes, and c and f show temperature tendencies. The Ames/Ames, Ames/KDM, KDM/Ames, KDM/KDM, TWOSTR/Ames, TWOSTR/KDM stand for combination of different radiative transfer equation solver and different *k*-distribution table. First and second symbols stand for radiative transfer equation solver and *k*-distribution table, respectively. The unit “K/sol” stands for the temperature change during a Martian solar day.

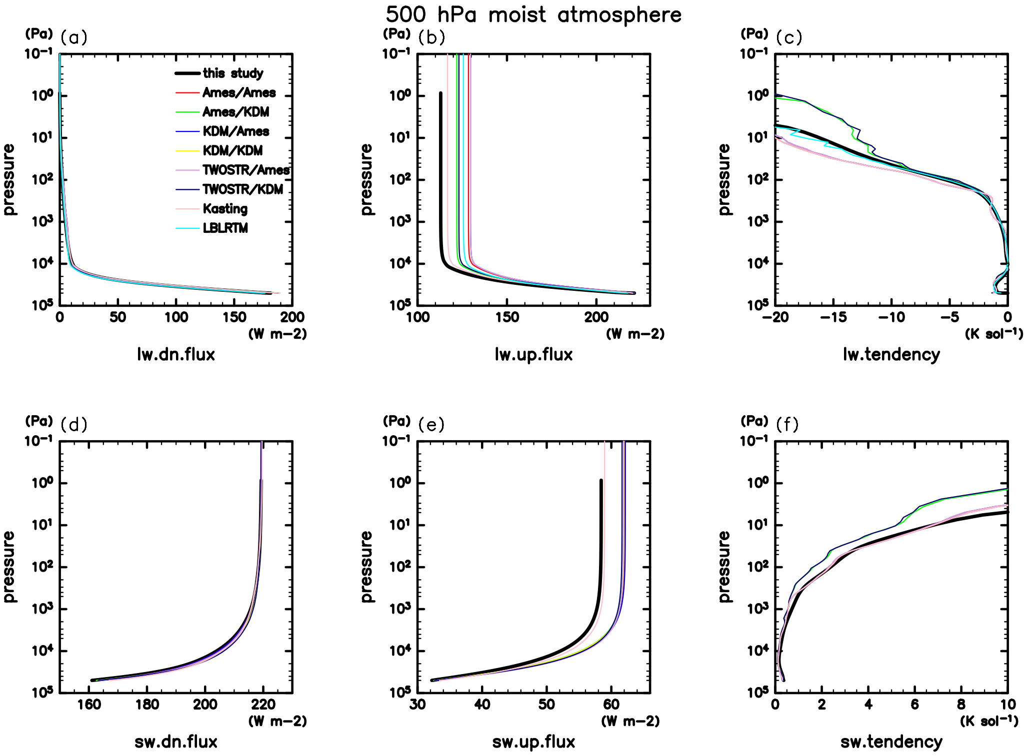

Fig. 18. Same as Fig. 17, but for the 500 hPa Mars moist atmosphere.

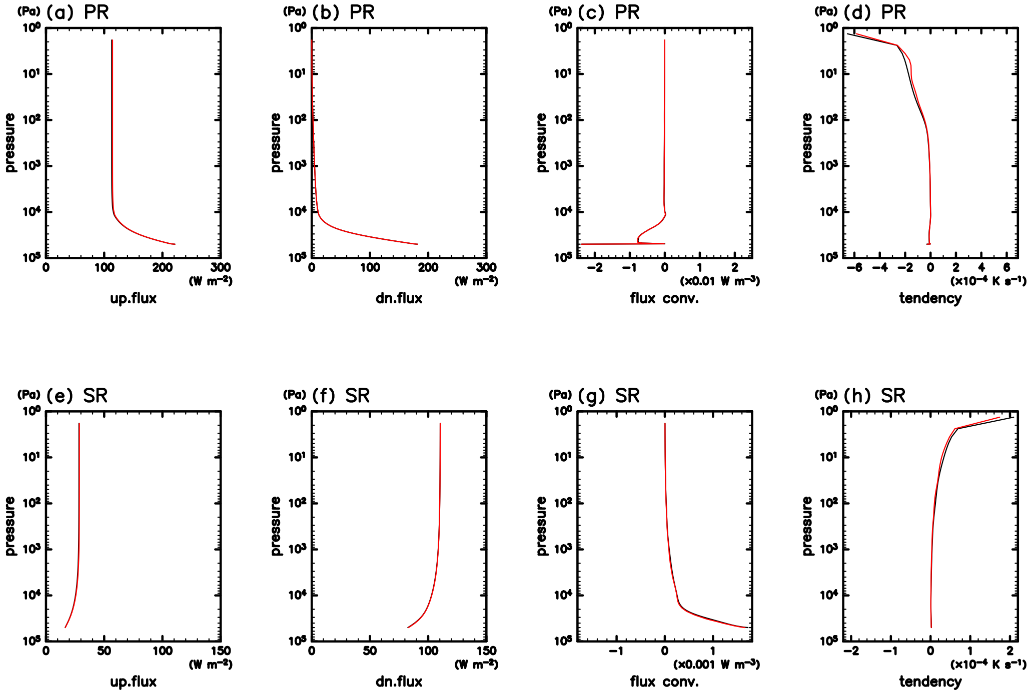

Fig. 19. Upward and downward radiative fluxes (a, e and b, f), flux convergences (c, g), and temperature tendencies (d, h) obtained by the line-by-line calculation (black) and the *k*-distribution calculation (red) for the 500 hPa Mars moist atmosphere. Panels a–d for planetary radiation and panels e–h for solar radiation.

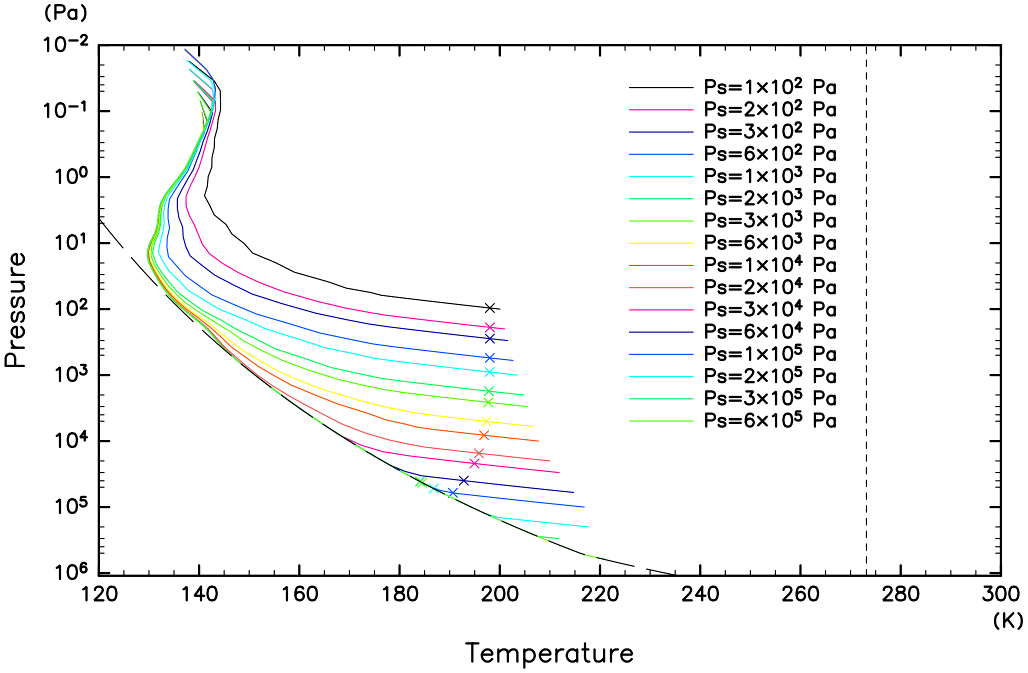

Fig. 20. Radiative-convective equilibrium temperature profiles for Mars. Long and short dashed lines show the CO_2 condensation temperature and a line of 273.15 K, respectively. Cross (×) markers show temperature whose black body radiation is equal to the outgoing planetary radiation.

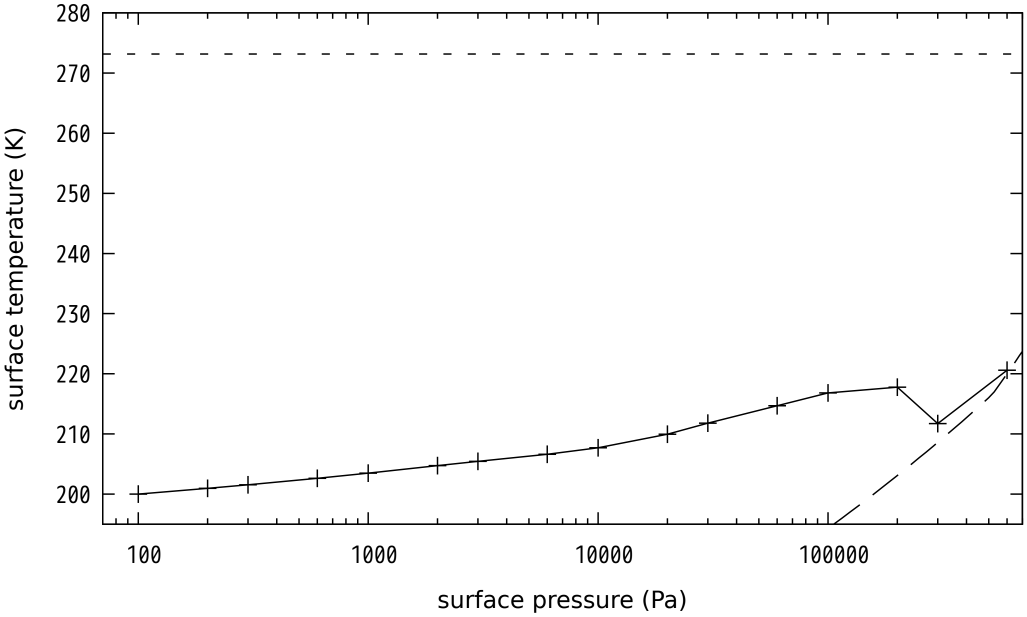

Fig. 21. Dependence of surface temperature on surface pressure obtained by radiative-convective equilibrium calculations for Mars. Long and short dashed lines show the CO_2 condensation temperature and a line of 273.15 K, respectively.

List of Tables

Table 1. Rayleigh scattering coefficient relative to that of air. The values are based on Rayleigh scattering cross-sections relative to H_2 presented by Pierrehumbert (2010).

	H_2O	N_2	O_2	CH_4
Rayleigh scattering coefficient relative to that of air	0.7578	1.0355	0.8690	2.2832

Table 2. Coefficients of CO_2 for absorption induced by collision with CO_2

wavenumber (cm^{-1})	references
1– 250	Gruszka and Borysow (1997)[a]
1100–2000	Baranov et al. (2004)
2650–3130	Stefani et al. (2013)
4000–5000	Marcq et al. (2006)
5000–6050	Bezard et al. (1990)
8363–9434	Bezard et al. (2011)

[a] The coefficient is obtained from Richard et al. (2012).

Table 3. “Absorption cross sections” of SO_2

wavenumber (cm^{-1})	references
23995–43985	Hermans et al. (2009)
43985–51000	Freeman et al. (1984)

Table 4.   Parameters of planetary atmospheres used in calculations

Planets	gravitational acceleration (m s^{-2})	specific heat at constant pressure (J K^{-1} kg^{-1})
Mars	3.72	746.7
Venus	8.9	837.6

Table 5. *k*-distribution table setting for Venus correlated *k*-distribution model. IP stands for integration point.

band number	wavenumber range (cm^{-1})	number of IPs in 0–0.98	number of IPs in 0.98–1
1	10– 255	6	1
2	255– 500	6	1
3	500– 600	6	1
4	600– 700	6	1
5	700– 840	6	1
6	840– 980	4	1
7	980– 1185	4	1
8	1185– 1390	4	1
9	1390– 1595	4	1
10	1595– 1800	4	1
11	1800– 2025	4	1
12	2025– 2250	4	1
13	2250– 2750	6	1
14	2750– 3250	6	1
15	3250– 4200	6	4
16	4200– 5150	6	4
17	5150– 6425	6	4
18	6425– 7700	6	4
19	7700–10275	6	4
20	10275–12850	6	4
21	12850–17750	4	1
22	17750–22650	4	1
23	22650–25825	4	1
24	25825–29000	4	1
25	29000–39500	4	1
26	39500–50000	1	1

Table 6. RMSEs of upward (Up) and downward (Dn) fluxes, flux convergences (FlxCnv), and temperature tendencies (Tend) for planetary radiation (PR) and solar radiation (SR) in the Venus calculation. Units of fluxes, flux convergences, and temperature tendencies are W m^{-2}, W m^{-3}, K s^{-1}, respectively.

	RMSE
UpPR	1.36×10^{-1}
DnPR	2.16×10^{-1}
FlxCnvPR	8.95×10^{-5}
TendPR	2.23×10^{-5}
UpSR	4.84×10^{-1}
DnSR	4.11×10^{-1}
FlxCnvSR	7.60×10^{-5}
TendSR	1.42×10^{-5}

Table 7. Global mean radiative fluxes for the VIRA. Up and Dn stand for upward and downward, respectively, PR and SR stand for planetary radiation and solar radiation, respectively. TOA and Sfc stand for the top of the atmosphere and the surface, respectively. Unit is W m^{-2}.

	UpPR	DnPR	UpSR	DnSR
TOA	154.3	—	500.5	656.9
Sfc	16575.8	16567.9	0.8	16.5

Table 8. Same as Table 7, but for the radiative-convective equilibrium profiles of Venus.

	Case V_A				Case V_B			
	UpPR	DnPR	UpSR	DnSR	UpPR	DnPR	UpSR	DnSR
TOA	157.2	—	501.7	658.8	150.9	—	508.0	658.7
Sfc	16098.7	16088.4	0.8	16.7	16816.3	16805.8	0.9	17.6

Table 9. Planetary radiation fluxes in the 2 bar pure CO_2 Mars atmosphere calculations. DnPR@SFC and UpPR@TOA stand for downward flux at the surface and upward flux at the top of the atmosphere, respectively. Unit is W m^{-2}.

	DnPR@SFC	UpPR@TOA
This study	177.6	93.7
This study but no SFT	182.0	90.5
Wordsworth et al. (2010)	–	88.2
Ramirez et al. (2014)	185.1	88.2
SMART[a]	178.4	88.4

[a] The values are shown in Ramirez et al. (2014).

Table 10. *k*-distribution table setting for Mars correlated *k*-distribution model. IP stands for integration point.

band number	wavenumber range (cm^{-1})	number of IPs in 0–0.98	number of IPs in 0.98–1
1	10– 150	8	8
2	150– 350	8	8
3	350– 500	8	8
4	500– 630	8	8
5	630– 700	8	8
6	700– 820	8	8
7	820– 1180	8	8
8	1180– 1660	8	8
9	1660– 2080	8	8
10	2080– 2600	8	8
11	2600– 3250	8	8
12	3250– 4000	8	8
13	4000– 5150	8	8
14	5150– 7700	8	8
15	7700–12850	8	8
16	12850–16000	1	1
17	16000–22650	1	1
18	22650–29000	1	1
19	29000–38000	1	1
20	38000–50000	1	1

Table 11. Same as Table 6, but for *k*-distribution calculation for 500 hPa Mars moist atmosphere.

	RMSE
UpPR	1.12
DnPR	9.40×10^{-2}
FlxCnvPR	6.13×10^{-5}
TendPR	1.10×10^{-5}
UpSR	3.14×10^{-1}
DnSR	1.87×10^{-1}
FlxCnvSR	2.15×10^{-5}
TendSR	3.98×10^{-6}